A warm Neptuneu2019s methane reveals core mass and vigorous atmospheric mixing

David K. Sing, Zafar Rustamkulov, Daniel P. Thorngren, Elena Manjavacas, Joanna K. Barstow, Pascal Tremblin, Catarina Alves de Oliveira, Stephan M. Birkmann, Pierre Ferruit, Tracy L. Beck, et al.

Article

A warm Neptune's methane reveals core mass and vigorous atmospheric mixing

https://doi.org/10.1038/s41586-024-07395-z

Received: 18 December 2023

Accepted: 5 April 2024

Published online: 20 May 2024

Open access

Check for updates

David K. Sing[1,2]✉, Zafar Rustamkulov[1], Daniel P. Thorngren[2], Joanna K. Barstow[3], Pascal Tremblin[4,5], Catarina Alves de Oliveira[6], Tracy L. Beck[7], Stephan M. Birkmann[6], Ryan C. Challener[8], Nicolas Crouzet[9], Néstor Espinoza[7], Pierre Ferruit[6], Giovanna Giardino[10], Amélie Gressier[7], Elspeth K. H. Lee[11], Nikole K. Lewis[8], Roberto Maiolino[12], Elena Manjavacas[2,13], Bernard J. Rauscher[14], Marco Sirianni[15] & Jeff A. Valenti[7]

Observations of transiting gas giant exoplanets have revealed a pervasive depletion of methane[1–4], which has only recently been identified atmospherically[5,6]. The depletion is thought to be maintained by disequilibrium processes such as photochemistry or mixing from a hotter interior[7–9]. However, the interiors are largely unconstrained along with the vertical mixing strength and only upper limits on the CH_4 depletion have been available. The warm Neptune WASP-107b stands out among exoplanets with an unusually low density, reported low core mass[10], and temperatures amenable to CH_4, though previous observations have yet to find the molecule[2,4]. Here we present a JWST-NIRSpec transmission spectrum of WASP-107b that shows features from both SO_2 and CH_4 along with H_2O, CO_2, and CO. We detect methane with 4.2σ significance at an abundance of 1.0 ± 0.5 ppm, which is depleted by 3 orders of magnitude relative to equilibrium expectations. Our results are highly constraining for the atmosphere and interior, which indicate the envelope has a super-solar metallicity of 43 ± 8 × solar, a hot interior with an intrinsic temperature of T_{int} = 460 ± 40 K, and vigorous vertical mixing which depletes CH_4 with a diffusion coefficient of $K_{zz} = 10^{11.6\pm0.1}$ cm^2 s^{-1}. Photochemistry has a negligible effect on the CH_4 abundance but is needed to account for the SO_2. We infer a core mass of $11.5^{+3.0}_{-3.6} M_\oplus$, which is much higher than previous upper limits[10], releasing a tension with core-accretion models[11].

We observed one transit of the exoplanet WASP-107b (ref. 12) with the G395H spectral grating of the James Webb Telescope Near-Infrared Spectrograph (JWST-NIRSpec) as part of Guaranteed Time Observations (GTO) programme 1224 (principal investigator S. Birkmann). In the first years of operation of the James Webb Space Telescope (JWST), this mode demonstrates reliable detections of H_2O, CO, CO_2 and SO_2 for several giant exoplanets[7,13–15]. See the Methods for further details on the observations and data analysis. The wavelength-integrated JWST-NIRSpec time-series photometry of WASP-107b is shown in Fig. 1, and the transmission spectrum is shown in Fig. 2. The spectrum shows several molecular absorption signals that are readily identifiable. We detect a large CO_2 absorption feature at 4.3 μm (ref. 15) (Fig. 2) and a slope-like feature at the shortest wavelengths from H_2O (ref. 14).

We ran a series of model retrievals to provide detailed constraints on the atmospheric composition and temperature (Methods). The H_2O and CO_2 features are detected at high confidence (Extended Data Table 2). The spectrum shows CO features between 4.5 μm and 5 μm (4σ), and an SO_2 absorption feature at 4.0 μm (5.5σ). SO_2 is a known by-product of photochemistry[7], which is generated when stellar ultra-violet radiation reacts with H_2S and has been identified in WASP-107b at longer wavelengths with JWST/MIRI[4]. Finally, a narrow CH_4 feature is identified at 3.32 μm (4.2σ). Although CH_4 has been unobservable at both shorter and longer wavelengths[2,4], the feature here is the Q-branch band head of CH_4, which is strong enough to appear above the clouds and H_2O (Fig. 2).

For H_2O, we find volume-mixing ratio abundances of $10^{-1.85\pm0.22}$, which indicates super-solar abundances near 40× solar. The presence of CO_2 is known to be a tracer of high metallicity[15,16], and the retrieved abundances of $10^{-3.33\pm0.27}$ support this, although these values are lower than the chemical equilibrium expectations by about an order of magnitude as the molecule is further sensitive to atmospheric mixing. CH_4 is also found to be heavily depleted, with retrieved abundances of $10^{-6.03\pm0.21}$. These CH_4 abundances are consistent with previous Hubble Space Telescope (HST) and JWST upper limits[2,4]. At the millibar pressures probed in transmission spectra, at 40× solar the atmosphere in equilibrium would be about one part in a thousand

[1]Department of Earth and Planetary Sciences, Johns Hopkins University, Baltimore, MD, USA. [2]Department of Physics and Astronomy, Johns Hopkins University, Baltimore, MD, USA. [3]School of Physical Sciences, The Open University, Milton Keynes, UK. [4]Université Paris-Saclay, UVSQ, CNRS, CEA, Maison de la Simulation, Gif-sur-Yvette, France. [5]Université Paris-Saclay, Université Paris Cité, CEA, CNRS, AIM, Gif-sur-Yvette, France. [6]European Space Agency, European Space Astronomy Centre, Madrid, Spain. [7]Space Telescope Science Institute, Baltimore, MD, USA. [8]Department of Astronomy and Carl Sagan Institute, Cornell University, Ithaca, NY, USA. [9]Leiden Observatory, Leiden University, Leiden, The Netherlands. [10]ATG Europe for the European Space Agency, ESTEC, Noordwijk, The Netherlands. [11]Center for Space and Habitability, University of Bern, Bern, Switzerland. [12]The Old Schools, University of Cambridge, Cambridge, UK. [13]AURA for the European Space Agency (ESA), Space Telescope Science Institute, Baltimore, MD, USA. [14]NASA Goddard Space Flight Center, Greenbelt, MD, USA. [15]European Space Agency (ESA) Office, Space Telescope Science Institute, Baltimore, MD, USA. ✉e-mail: dsing@jhu.edu

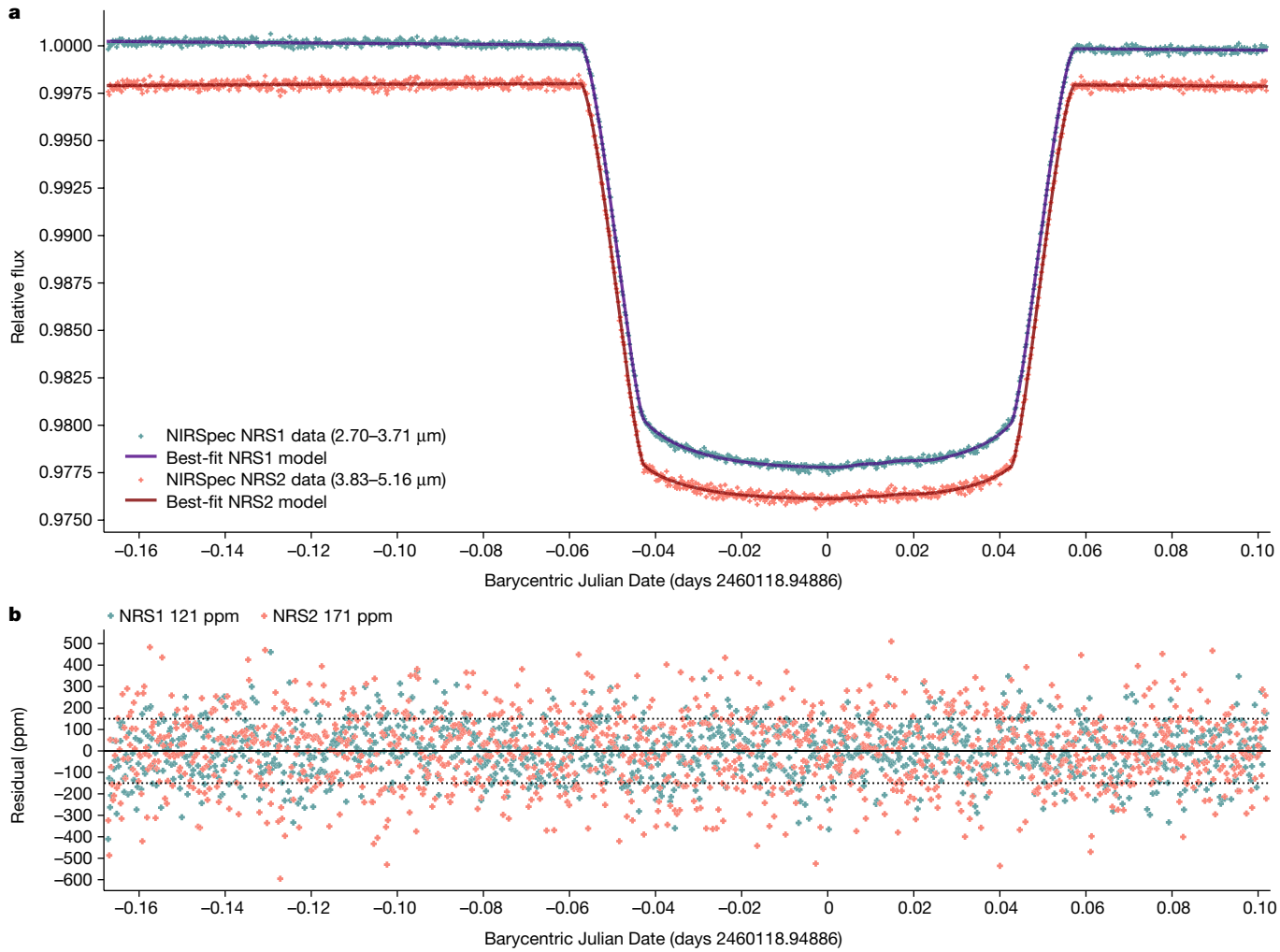

Fig. 1 | The light curve of WASP-107b observed by JWST-NIRSpec G395H. **a**, The normalized wavelength-integrated white-light curves for the two detectors are shown, with the NRS1 (2.70–3.71 μm) and NRS2 (3.83–5.16 μm) detectors offset for clarity. A best-fit limb-darkened transit model is overplotted (blue). See Extended Data Fig. 2 for further details. **b**, The model residuals that achieve near-photon limited precisions.

CH_4, whereas abundances slightly less than 1 part per million (ppm) are found. Measuring the amount of CH_4 depletion is highly constraining for non-equilibrium models[8], as it can be tied to the pressure and temperature of the hotter interior from which the species is mixed to higher levels. Although not every planet shows a CH_4 depletion[5], for those that do such as WASP-107b (ref. 4) and others[3], only the upper limits on the depletion are available. By quantifying the CH_4 depletion, the non-equilibrium chemistry can be tightly constrained and the depletion mechanisms can be explored. We find abundances of SO_2 to be $10^{-5.06\pm0.13}$, which broadly match the JWST/MIRI results[4] as well as those of WASP-39 b (refs. 7,17) indicating ongoing photochemistry in the atmosphere.

Given the retrieved molecular abundances, we ran a grid of forward atmospheric models to place constraints on the photochemistry, vertical mixing, metallicity and temperature structure of the planet. The model includes non-equilibrium chemistry from both vertical mixing and photochemistry self-consistently calculated[18,19] (Methods). The chemistry was computed using T–P profiles in radiative–convective equilibrium, with a range of intrinsic temperatures, T_{int}. The intrinsic temperature is related to the emitted flux generated from the interior of the planet, which passes through the atmosphere, with Jupiter having a T_{int} near 100 K. With vertical mixing, most of the molecular species detected are expected to be uniformly mixed from their quench pressures at deeper and hotter conditions in chemical equilibrium to higher altitudes. We modelled the vertical mixing in a turbulent flow using the vertical eddy diffusion coefficient, K_{zz}. Our best-fit forward model to the retrieved abundances is shown in Fig. 3 (see also Extended Data Fig. 7). We find the combination of H_2O, CO, CO_2, CH_4 and SO_2 to be highly constraining. H_2O and CO are insensitive to non-equilibrium chemistry in this temperature regime (Fig. 3) helping to uniquely measure the metallicity, whereas the combination of CO_2 and CH_4 are jointly sensitive to K_{zz} and T_{int}. SO_2 also helps to provide an upper bound on K_{zz} (Extended Data Fig. 7). With these combined constraints, the forward model grid indicates the planet has a hot intrinsic temperature of $T_{int} = 460 \pm 40$ K, a high metallicity of $Z = 43 \pm 8\times$ solar and vigorous vertical mixing with a $K_{zz} = 10^{11.6\pm0.1}$ cm^2 s^{-1}.

Theoretical models have estimated the strength of vertical mixing and K_{zz} (refs. 20–22). However, the overall uncertainty on K_{zz} for giant planets remains large[23], with values often ranging from 10^4 cm^2 s^{-1} to 10^{12} cm^2 s^{-1} for hot Jupiters[8]. The empirical constraints on K_{zz} for exoplanets currently rely on broadband Spitzer/IRAC photometry[9], in which there is considerable planet-to-planet stochasticity and the molecular features are spectroscopically unresolved, giving rise to modelling degeneracies. The K_{zz} measurement in WASP-107b here is a substantial improvement over the order of magnitude estimates previously explored using either the upper limits on CH_4 from JWST/MIRI[4] or population-level results[9]. The measurement is one of the

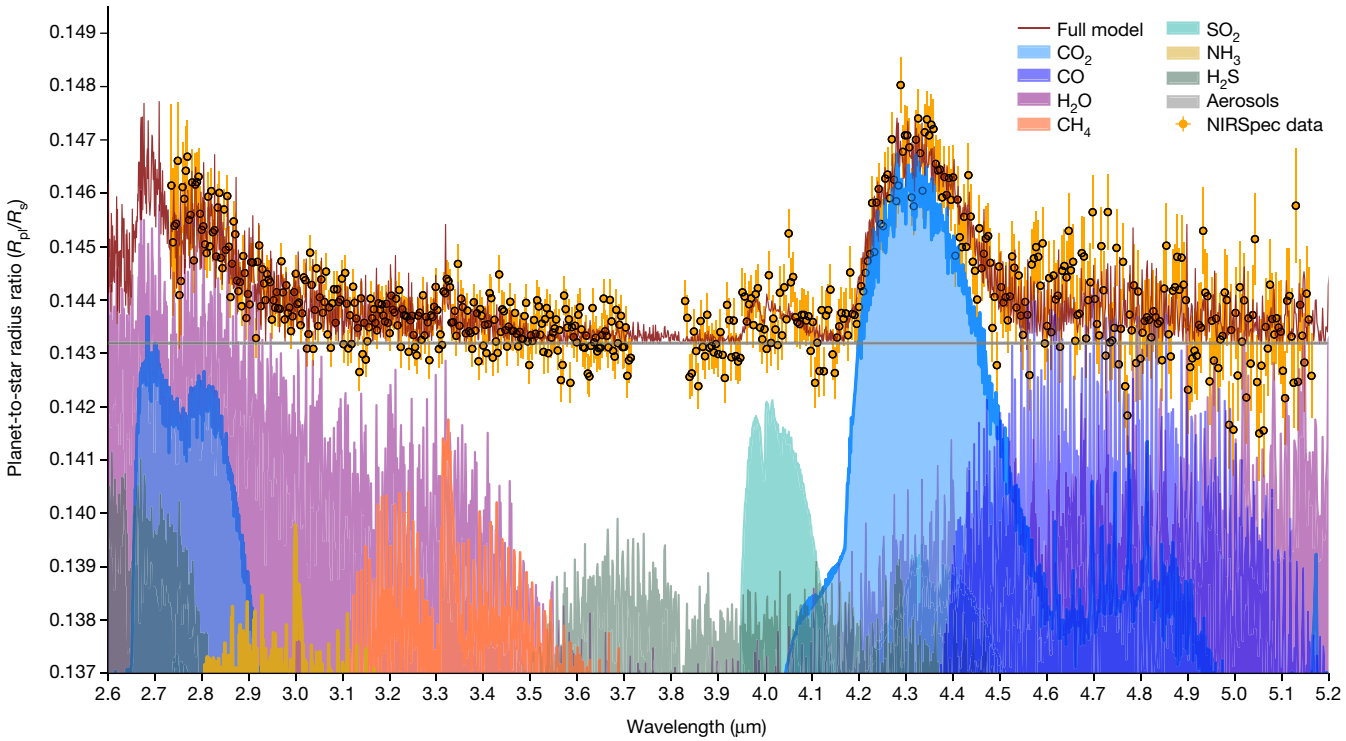

Fig. 2 | WASP-107b transmission spectral measurements. JWST-NIRSpec transmission spectrum and the 1σ uncertainties. The best-fit ATMO[32] model is also plotted, and the individual contributions for each molecular species are shown.

best evidence so far that non-equilibrium chemistry from vertical mixing is an important physical process in exoplanetary atmospheres, a mechanism long known to be important for Jupiter[24]. The K_{zz} value for WASP-107b at 1 bar is about 1,000–10,000 times higher than the typical estimates used[7,25], which are largely based on three-dimensional general circulation models (GCM)[20]. This could indicate the planet has anomalously high vertical mixing, perhaps because of the high T_{int} resulting in a convective region that reaches lower than expected pressures. Alternatively, the GCMs may be inadequately capturing the eddy dissipation with the artificial viscosity parameters used[26].

The high T_{int} is a direct constraint on the energy stored in the deep atmosphere, which can help us understand the mechanism responsible for the inflated radius of the planet. The anomalously large radii of irradiated warm Neptunes and hot Jupiters are one of the most intriguing and long-standing problems in our understanding of extrasolar

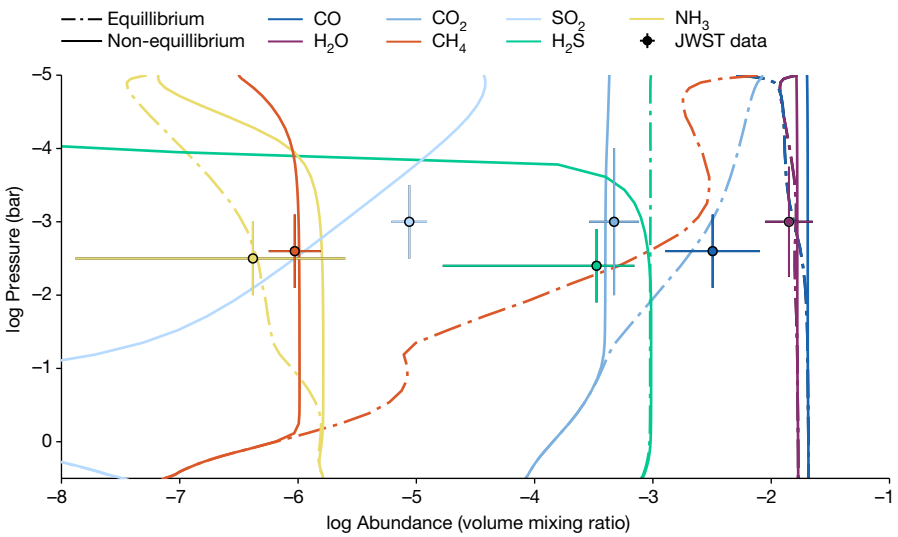

Fig. 3 | Model interpretation. ATMO non-equilibrium chemistry model with vertical mixing and photochemistry. The best-fit non-equilibrium chemistry model (solid lines) and the abundance profiles in equilibrium (dot-dashed lines) are shown. The retrieved JWST abundances are shown (data points) with the model grid indicating that the planet has hot interior temperatures ($T_{int} = 458 \pm 38$ K), a super-solar metallicity ($Z/Z_{\odot} = 43 \pm 8$) with vigorous vertical mixing ($K_{zz} = 10^{11.6 \pm 0.1}$ cm^2 s^{-1}).

giant planets with several proposed mechanisms, including tidal heating[27], downward transport of kinetic energy[28], enhanced opacities[29], ongoing layered convection[30], ohmic dissipation[31] and, more recently, the advection of potential temperature[32,33]. The potential temperature mechanism has been recently demonstrated in the hot Jupiter WASP-76 b using first-principle radiative GCM simulations[34]. The hot interior temperature can explain the higher vertical mixing rates, as both hotter temperatures and lower surface gravities are expected to increase K_{zz}. These high vertical mixing rates with super-solar metallicities and hot intrinsic temperatures also explain the cloud properties observed, in which silicate cloud particles were found with JWST/MIRI[4]. For planets such as WASP-107b with equilibrium temperatures near 770 K, the condensation of silicate clouds should be occurring at high unobservable pressures if $T_{\rm int}$ was low (about 100 K) (ref. 8). However, with a high $T_{\rm int}$ of 460 K, the silicate cloud base is moved to about bar pressures (Extended Data Fig. 6) and the high K_{zz} values found here are more than sufficient to aloft the cloud particles to mbar pressures in which they are observed in transmission.

The mass, radius and $T_{\rm int}$ alone constrain the overall bulk metallicity of the planet to be $Z_{\rm p} = 63.5^{+10.4}_{-8.5}$%. A precise atmospheric metallicity and $T_{\rm int}$ enable us to place better constraints on the overall metal content of the planet and estimate the core mass of the planet (Methods). So far, no gas giant exoplanet has had the presence of a core significantly detected, with upper limits reported for HAT-P-13 b (ref. 35) and WASP-107b (ref. 10). Any metals seen in the bulk but not in the atmosphere must be hidden in the interior in a core or composition layers. Assuming a uniform composition core, an isothermal 50:50% mixture of rock and water, gives us $M_{\rm c} = 11.5^{+3.0}_{-3.6} M_{\oplus}$—which is one-third of the mass of the planet and the first statistically significant core detection for a giant exoplanet. This value is much higher than the previous estimates limiting the core to less than $4.6 M_{\oplus}$ (ref. 10), which had assumed the planet followed a standard cooling track with no tidal heating. These low core-mass values were in tension with standard core-accretion models[11] that do not predict such a light core could accrete the massive H/He envelope observed. By contrast, our core-mass estimate matches the approximately $10 M_{\oplus}$ prediction needed to elicit runaway gas accretion within the lifetime of the disks. It is worth noting that the structure of the interior may not be exactly an envelope-on-core model, but may be more like Neptune and Uranus with a rocky core and an icy water mantle[36] or the core may be diffuse and/or similar to that of Jupiter[37,38]. The core-mass result should be understood as the total excess non-H/He heavy elements in the interior, irrespective of how exactly it is structured. With the proof-of-concept demonstrated here, using CH_4 depletion as a thermometer of the deep atmosphere for other gas giant exoplanets could help provide constraints at the population level about how planetary cores might differ with planet or host-star mass and metallicities.

WASP-107b is one of the lowest-density planets known, which has led to speculation that the planet has formed substantially different from the solar system, with dust-free accretion or in situ scenarios explored[10]. However, the important bulk properties found here line up well with the planets of the solar system (SS) indicating a similar core-accretion scenario. In particular, with a metallicity of $43 \pm 8 \times$ solar, WASP-107b is close to the mass-metallicity trend of the gas giant SS planets[39]. Moreover, with an estimated core mass of $11.48^{+3.0}_{-3.6} M_{\oplus}$, WASP-107b is also intermediate between Neptune and Saturn, falling reasonably along their lines of formation[40,41]. The main difference for WASP-107b seems to be its much hotter interior, resulting in an extremely puffy planet.

Online content

Any methods, additional references, Nature Portfolio reporting summaries, source data, extended data, supplementary information, acknowledgements, peer review information; details of author contributions and competing interests; and statements of data and code availability are available at https://doi.org/10.1038/s41586-024-07395-z.

1. Stevenson, K. B. et al. Possible thermochemical disequilibrium in the atmosphere of the exoplanet GJ 436b. *Nature* **464**, 1161–1164 (2010).
2. Kreidberg, L., Line, M. R., Thorngren, D., Morley, C. V. & Stevenson, K. B. Water, high-altitude condensates, and possible methane depletion in the atmosphere of the warm super-Neptune WASP-107b. *Astrophys. J. Lett.* **858**, L6 (2018).
3. Fu, G. et al. Water and an escaping helium tail detected in the hazy and methane-depleted atmosphere of HAT-P-18b from JWST NIRISS/SOSS. *Astrophys. J. Lett.* **940**, L35 (2022).
4. Dyrek, A. et al. SO_2, silicate clouds, but no CH_4 detected in a warm Neptune. *Nature* **625**, 51–54 (2024).
5. Bell, T. J. et al. Methane throughout the atmosphere of the warm exoplanet WASP-80b. *Nature* **623**, 709–712 (2023).
6. Madhusudhan, N. et al. Carbon-bearing molecules in a possible Hycean atmosphere. *Astrophys. J. Lett.* **956**, L13 (2023).
7. Tsai, S.-M. et al. Photochemically produced SO_2 in the atmosphere of WASP-39b. *Nature* **617**, 483–487 (2023).
8. Fortney, J. J. et al. Beyond equilibrium temperature: how the atmosphere/interior connection affects the onset of methane, ammonia, and clouds in warm transiting giant planets. *Astron. J.* **160**, 288 (2020).
9. Baxter, C. et al. Evidence for disequilibrium chemistry from vertical mixing in hot Jupiter atmospheres. A comprehensive survey of transiting close-in gas giant exoplanets with warm-*Spitzer*/IRAC. *Astron. Astrophys.* **648**, A127 (2021).
10. Piaulet, C. et al. WASP-107b's density is even lower: a case study for the physics of planetary gas envelope accretion and orbital migration. *Astron. J.* **161**, 70 (2021).
11. Pollack, J. B. et al. Formation of the giant planets by concurrent accretion of solids and gas. *Icarus* **124**, 62–85 (1996).
12. Anderson, D. R. et al. The discoveries of WASP-91b, WASP-105b and WASP-107b: two warm Jupiters and a planet in the transition region between ice giants and gas giants. *Astron. Astrophys.* **604**, A110 (2017).
13. Birkmann, S. M. et al. The Near-Infrared Spectrograph (NIRSpec) on the James Webb Space Telescope IV. Capabilities and predicted performance for exoplanet characterization. *Astron. Astrophys.* **661**, A83 (2022).
14. Alderson, L. et al. Early Release Science of the exoplanet WASP-39b with JWST NIRSpec G395H. *Nature* **614**, 664–669 (2023).
15. The JWST Transiting Exoplanet Community Early Release Science Team. Identification of carbon dioxide in an exoplanet atmosphere. *Nature* **614**, 649–652 (2023).
16. Moses, J. I., Madhusudhan, N., Visscher, C. & Freedman, R. S. Chemical consequences of the C/O ratio on hot Jupiters: examples from WASP-12b, CoRoT-2b, XO-1b, and HD 189733b. *Astrophys. J.* **763**, 25 (2013).
17. Rustamkulov, Z. et al. Early Release Science of the exoplanet WASP-39b with JWST NIRSpec PRISM. *Nature* **614**, 659–663 (2023).
18. Drummond, B. et al. The effects of consistent chemical kinetics calculations on the pressure-temperature profiles and emission spectra of hot Jupiters. *Astron. Astrophys.* **594**, A69 (2016).
19. Nicholls, H., Hébrard, E., Venot, O., Drummond, B. & Evans, E. Temperature-chemistry coupling in the evolution of gas giant atmospheres driven by stellar flares. *Mon. Not. R. Astron. Soc.* **523**, 5681–5702 (2023).
20. Parmentier, V., Showman, A. P. & Lian, Y. 3D mixing in hot Jupiters atmospheres. I. Application to the day/night cold trap in HD 209458b. *Astron. Astrophys.* **558**, A91 (2013).
21. Zhang, X. & Showman, A. P. Global-mean vertical tracer mixing in planetary atmospheres. I. Theory and fast-rotating planets. *Astrophys. J.* **866**, 1 (2018).
22. Menou, K. Turbulent vertical mixing in hot exoplanet atmospheres. *Mon. Not. R. Astron. Soc.* **485**, L98–L103 (2019).
23. Mukherjee, S. et al. Probing the extent of vertical mixing in brown dwarf atmospheres with disequilibrium chemistry. *Astrophys. J.* **938**, 107 (2022).
24. Prinn, R. G. & Barshay, S. S. Carbon monoxide on Jupiter and implications for atmospheric convection. *Science* **198**, 1031–1034 (1977).
25. Moses, J. I., Tremblin, P., Venot, O. & Miguel, Y. Chemical variation with altitude and longitude on exo-Neptunes: predictions for Ariel phase-curve observations. *Exp. Astron.* **53**, 279–322 (2022).
26. Mayne, N. J. et al. The unified model, a fully-compressible, non-hydrostatic, deep atmosphere global circulation model, applied to hot Jupiters: ENDGame for a HD 209458b test case. *Astron. Astrophys.* **561**, A1 (2014).
27. Bodenheimer, P., Lin, D. N. C. & Mardling, R. A. On the tidal inflation of short-period extrasolar planets. *Astrophys. J.* **548**, 466–472 (2001).
28. Showman, A. P. & Guillot, T. Atmospheric circulation and tides of "51 Pegasus b-like" planets. *Astron. Astrophys.* **385**, 166–180 (2002).
29. Burrows, A., Hubeny, I., Budaj, J. & Hubbard, W. B. Possible solutions to the radius anomalies of transiting giant planets. *Astrophys. J.* **661**, 502–514 (2007).
30. Chabrier, G. & Baraffe, I. Heat transport in giant (exo)planets: a new perspective. *Astrophys. J. Lett.* **661**, L81–L84 (2007).
31. Batygin, K., Stevenson, D. J. & Bodenheimer, P. H. Evolution of ohmically heated hot Jupiters. *Astrophys. J.* **738**, 1 (2011).
32. Tremblin, P. et al. Advection of potential temperature in the atmosphere of irradiated exoplanets: a robust mechanism to explain radius inflation. *Astrophys. J.* **841**, 30 (2017).
33. Sainsbury-Martinez, F. et al. Idealised simulations of the deep atmosphere of hot Jupiters: deep, hot adiabats as a robust solution to the radius inflation problem. *Astron. Astrophys.* **632**, A114 (2019).

34. Sainsbury-Martinez, F. et al. Evidence of radius inflation in radiative GCM models of WASP-76b due to the advection of potential temperature. *Mon. Not. R. Astron. Soc.* **524**, 1316–1325 (2023).
35. Buhler, P. B. et al. Dynamical constraints on the core mass of hot Jupiter HAT-P-13b. *Astrophys. J.* **821**, 26 (2016).
36. Cavalié, T. et al. The deep composition of Uranus and Neptune from in situ exploration and thermochemical modeling. *Space Sci. Rev.* **216**, 58 (2020).
37. Vazan, A., Helled, R. & Guillot, T. Jupiter's evolution with primordial composition gradients. *Astron. Astrophys.* **610**, L14 (2018).
38. Debras, F. & Chabrier, G. New models of Jupiter in the context of *Juno* and *Galileo*. *Astrophys. J.* **872**, 100 (2019).
39. Thorngren, D. P., Fortney, J. J., Murray-Clay, R. A. & Lopez, E. D. The mass-metallicity relation for giant planets. *Astrophys. J.* **831**, 64 (2016).
40. Guillot, T. et al. Giant planets from the inside-out. Preprint at https://arxiv.org/abs/2205.04100 (2022).
41. Mankovich, C. R. & Fuller, J. A diffuse core in Saturn revealed by ring seismology. *Nat. Astron.* **5**, 1103–1109 (2021).

Methods

Data reduction

A transit of WASP-107b was observed on 23 June 2023 with JWST for 6.5 h using the NIRSpec instrument with the G395H grating. This setup gives a wavelength range from 2.7 μm to 5.18 μm with the corresponding resolving power ranging between 1,828 and 3,600. The instrument used the NRSRAPID readout pattern and SUB2048 subarray with 20 groups per integration, resulting in 1,230 integrations over the 6.5-h observation.

FIREFLy

We reduce the data using the Fast Infrared Exoplanet Fitting Lightcurve (FIREFLy)[17,42] reduction suite, which starts with a customized reduction using the STScI pipeline and the uncalibrated images. Our custom reduction includes 1/*f* destriping at the group level before the ramp is fit. The jump-step and dark-current stages of the STScI pipeline were skipped. We then use the custom-run pipeline two-dimensional (2D) images after the gain scale step and perform customized cleaning of bad pixels, cosmic rays and hot pixels. Using cross-correlation, we measured the positional shift of the spectral trace across the detector and performed shift stabilization of the images with flux-conserving interpolation. This procedure has been found to reduce the amplitude of position-dependent trends[17,42], as the underlying stellar spectra do not shift in wavelength across a pixel through the time series. We note that nearly identical results can be found if shift stabilization of the data is not performed and the extraction window is moved instead. Further position-dependent trends can be expected from intrapixel sensitivity variations[13], although their magnitude on-sky has been very small as JWST generally has excellent pointing with the detector shifts found in this dataset to be of the order of about 1/1,000 of a pixel. We optimized the width of our flux-extraction aperture to minimize the standard deviation of the white-light curve photometry and extracted the spectrophotometric time series. The 2D extracted spectral time series can be seen in Extended Data Fig. 1. We extracted the transmission spectra with a range of different wavelength bin sizes, reporting an extraction with a resolution near $R = 950$.

We fit the transit light curves using a quadratic function to model stellar limb darkening given as

$$\frac{I(\mu)}{I(1)} = 1 - a(1-\mu) - b(1-\mu)^2, \quad (1)$$

where $I(1)$ is the intensity at the centre of the stellar disk, $\mu = \cos(\theta)$, where θ is the angle between the line of sight and the emergent intensity, and a and b are the limb-darkening coefficients. In practice, we remap a and b and fit instead for q_1 and q_2, which is shown to be less degenerate[43]. The resulting limb-darkening coefficients can be seen in Extended Data Fig. 3 with the best-fit orbital parameters given in Extended Data Table 1. Model limb-darkening coefficients calculated from three-dimensional models[44] capture the wavelength dependence of limb darkening well, but we find an overall offset in the coefficients of −0.0378 and +0.175 for q_1 and q_2, respectively. We applied these offsets to the wavelength-dependent model limb-darkening coefficients and re-fit the transmission spectra with fixed limb darkening. This iterative procedure reduces the bin-to-bin scatter of the transmission spectra as the limb darkening is fixed, but allows for overall differences between the transit data and stellar model limb darkening. We bin the spectrophotometry into 576 wavelength bins, providing a spectral resolution of $R \approx 950$ for the planet.

Stellar spot crossing

A stellar spot-crossing event is observed in our transit light curve data, appearing in both NRS1 and NRS2 shortly after mid-transit, which we decontaminated from the light curves and the transmission spectrum. The host star is known to be modestly active[12], with optical photometric modulations of around 0.4% over a period of about 17 days. We modelled this spot empirically, first fitting the non-spotted region with a transit light curve and using the overall residual in the spotted region to define the photometric shape of the spot (Extended Data Fig. 2). A Gaussian filter was then applied to the spot shape and subsequently used to model the full transit light curves, fitting for a scaling factor. As the spot is low in amplitude and covers only a small portion of the data, our overall transmission spectrum is insensitive to the occulted spot. We found equivalent results between masking the region for all the transit light curve fits and fitting for the spot shape in the light curves.

TEATRO

An independent data reduction was performed using the Transiting Exoplanet Atmosphere Tool for Reduction of Observations (TEATRO) (https://github.com/ncrouzet/TEATRO) pipeline.

The data were processed using the jwst calibration software package v.1.10.2, CRDS v.11.16.19, CRDS context 1147 (refs. 45,46), starting from the 'uncal' files. For stage 1, a jump rejection threshold of 6 was used and the 'jump.flag_4_neighbors' parameter was turned off. For stage 2, the flat field and photometric calibration steps were skipped. Bad pixels and missing pixels were then corrected in each integration. The centre of the spectral trace in the spatial direction was computed by fitting a Gaussian function to each column and fitting a third-order polynomial to their maxima. For each integration, the background was computed on a column-by-column basis using pixels above and below the spectral trace (or only one of them at the short- and long-wavelength edges of NRS2). An aperture half-width of 2.73 and 3 pixels and background regions starting 6.5 and 6 pixels further away were used for nrs1 and nrs2, respectively. The background subtraction and spectral extraction were performed using the 'extract_1d' routine with the corresponding polynomial coefficients as parameters. The white-light flux was computed using the 'white_light' step routine. For the spectroscopic analysis, we binned the spectra in 86 and 136 wavelength bins of 0.01 μm width, covering the 2.86–3.72 μm and 3.82–5.18 μm ranges with nrs1 and nrs2, respectively. The light curves were normalized by the out-of-transit flux and a five-iteration 3.5 sigma-clipping was applied to remove the outliers.

Light-curve fits were performed using the exoplanet[47,48] package with a quadratically limb-darkened transit light-curve model and a second-order polynomial to account for long-term trends. A fit to the white-light curve obtained from NRS1 only was first performed to derive system parameters (mid-transit time, impact parameter, planet-to-star radius ratio and stellar density). These parameters were then fixed for the spectroscopic light-curve fits, leaving only the radius ratio and polynomial trend as free parameters. Limb-darkening coefficients were obtained from ExoTETHyS[49]; they were free for the white-light curve fit and fixed for the spectroscopic light-curve fits. The median of the posterior distribution of the radius ratio was used to derive the transit depth in each wavelength bin. The uncertainties were computed by summing quadratically the standard deviations of the in- and out-of-transit parts of the light curve divided by the square root of their respective number of points (this gave a better estimate than the standard deviation of the posterior distributions).

Comparing the TEATRO reduction to FIREFLy, we find good consistency with the spectra agreeing at the point-to-point level at better than 1σ for both NRS1 and NRS2.

Resolution-linked bias

We have adjusted the retrieved abundance to account for the resolution-linked bias (RLB) effect[50], in which planetary absorption signatures are diluted within stellar absorption lines. For G395H data, this, in particular, dilutes the transmission spectral signatures of CO, as the molecule is found in the atmosphere of both the star and planet. We followed

the method in ref. 42, estimating the magnitude of the effect using high-resolution models. Compared with WASP-39A, WASP-107A is a cooler later-type star that enhances the RLB effect as the stellar CO is stronger. However, within the CO lines, the atmosphere of the planet is cloudier than WASP-39b, which reduces the effect. In total, we find that the RLB reduces the inferred CO abundance by 0.2 dex, which is about half of the uncertainty in the CO abundance.

Atmospheric models

ATMO setup. We use ATMO, a one-dimensional (1D)–2D radiative–convective equilibrium model for planetary atmospheres to generate models of WASP-107b. More comprehensive descriptions of the model can be found in refs. 18,32,51–54. The ATMO model is used here as both a forward physical model in radiative and chemical (dis-)equilibrium and a retrieval model in which the abundances and temperature–pressure (T–P) profile are let free to fit the data. By comparing the retrieved and forward model abundances within a single model suite, model-to-model systematics from such sources as differences in opacities can be avoided. ATMO has been validated against the publicly available MET office radiative transfer code SOCRATES[55] and has been benchmarked against Exo-REM[56] and petitCODE[57] in the context of JWST observations[58].

ATMO solves the radiative transfer equation with isotropic scattering in 1D plane-parallel geometry for the irradiation and thermal emission, finding a pressure–temperature (P–T) profile that satisfies hydrostatic equilibrium and conservation of energy and is also self-consistent with the atmospheric chemistry and opacities, given a set of elemental abundances. The total opacity of the gas mixture is computed using the correlated-k approximation using the random overlap method with resorting and rebinning[51,59]. The k-coefficients are calculated 'on the fly' for each atmospheric layer, spectral band and iteration such that the derived opacities are physically self-consistent with the T–P profile and chemical composition. ATMO can also be used as a full line-by-line code at high spectral resolution, although that is not used here as it is too computationally heavy for spectral retrieval purposes. The spectrally active species currently include H_2–H_2 and H_2–He collision-induced absorption (CIA) opacities, as well as H_2O, CO_2, CO, CH_4, NH_3, Na, K, Li, Rb, Cs, TiO, VO, Fe, FeH, CrH, PH_3, HCN, C_2H_2, H_2S, SO_2 and H− (see refs. 54,60 for full description). Multi-gas Rayleigh scattering contributions from the different species are also included.

The chemical abundances in equilibrium are determined by minimizing the Gibbs free energy following the method in ref. 61 and using the thermochemical data from ref. 62. Solar elemental abundances are set from refs. 63,64, with the chemistry fully flexible for any mix of input elemental abundances. This method also enables the depletion of gas phase species because of condensation as well as thermal ionization and dissociation. ATMO has several different chemical schemes that can be chosen and, by default, calculates the abundances for 175 neutral, 9 ionic and 93 condensate species. Condensation can be treated locally or with rainout. Rainout is treated by calculating the chemistry at the highest pressure initially, then following the T–P profile towards lower pressures. Condensed elements are removed locally, as well as for all lower pressures[65], allowing for opacity changes that can alter the radiative–convective balance and P–T profile.

For non-equilibrium C–H–N–O chemistry, ATMO uses a chemical kinetics scheme from ref. 66 as described in ref. 18. As done in ref. 7 to model the S photochemistry of WASP-39b with ATMO, we used the thermochemical network from ref. 67 along with the photochemical scheme from ref. 68, including 71 photolysis reactions of H_2S, S_2, SO_2, SO, SO_2, CH_3SH, SH, H_2SO and COS.

ATMO includes a relatively simple treatment of clouds and hazes[54] and does not consider the distribution of aerosol particles. An aerosol 'haze' scattering is implemented as enhanced Rayleigh-like scattering[69], presented as

$$\sigma(\lambda)_{\mathrm{haze}} = \delta_{\mathrm{haze}}\sigma_0(\lambda/\lambda_0)^{-\alpha_{\mathrm{haze}}}, \quad (2)$$

where $\sigma(\lambda)$ is the total scattering cross-section of the material, δ_{haze} is an empirical enhancement factor, σ_0 is the scattering cross-section of molecular hydrogen at 0.35 μm and α_{haze} is a factor determining the wavelength dependence with $\alpha_{\mathrm{haze}} = 4$ corresponding to Rayleigh scattering. Condensate 'cloud' absorption is assumed to have a grey wavelength dependence and is calculated as

$$\kappa(\lambda)_{\mathrm{cloud}} = \delta_{\mathrm{cloud}}\kappa_{H_2}, \quad (3)$$

where $\kappa(\lambda)_{\mathrm{cloud}}$ is the 'cloud' absorption opacity, δ_{cloud} is an empirical factor governing the strength of the grey scattering and κ_{H_2} is the scattering opacity due to H_2 at 0.35 μm. $\sigma(\lambda)_{\mathrm{haze}}$ and $\kappa(\lambda)_{\mathrm{cloud}}$ are added to the total gaseous scattering and absorption, respectively.

For spectra retrievals, we coupled the forward ATMO model to a nested sampling statistical algorithm to marginalize the posterior distribution and measure the model evidence[70–72]. The retrieval aspects of ATMO were developed to fit transit and eclipse data, with results published for several transiting planets[3,73–77]. A main difference compared with the forward models is that the retrieval does not converge the T–P profile to radiative–convective equilibrium, but rather parameterizes the profile that is then fit against the planetary spectrum. With the retrieval model, the k-coefficients are still calculated 'on the fly' in the same way as described in the forward model (and equilibrium chemistry if specified) for every likelihood evaluation step to maximize accuracy and consistency. To parameterize the T–P profile, we use the three-channel (two optical, one infrared) analytic radiative equilibrium model as described in ref. 78, which is based on the derivations in ref. 79.

ATMO WASP-107b retrievals. For the NIRSpec WASP-107b data, we found the flexible parameterized P–T profile simply fit to a simple isotherm, so we instead fit for a single isothermal temperature for the atmosphere. Given the atmosphere of the planet is far out of equilibrium, we fit a constant VMR for each molecule. Apart from the cloud, we included the spectrally active species of H_2–H_2, H_2–He (CIA) opacities, H_2O (ref. 80), CO_2 (ref. 81), CO (ref. 82), CH_4 (ref. 83), NH_3 (ref. 84), H_2S (ref. 85) and SO_2 (ref. 86).

We searched the G395H data for H_2S and can marginally improve the model fits to the data, but the inclusion of the model is not supported with confidence by the Bayesian evidence. Considerable opacity from aerosols is also needed to fit the spectrum, which is in line with previous HST results in which H_2O and He features are observed between 0.9 μm and 1.6 μm peaking above the clouds[2,75]. We fit the data with a grey cloud and a scattering haze but found only a grey cloud was needed to fit the data (Extended Data Table 3). Moreover, the choice of cloud parameterization did not have a strong influence on the retrieved abundances. Fitting the grey cloud either with a single uniform opacity or for a cloud-top pressure also gave similar results. A narrow feature of NH_3 is potentially found in the data at 3.0 microns, but similar to H_2S, its identification is not supported with high confidence by the Bayesian evidence. NH_3 has been marginally detected at longer wavelengths with JWST/MIRI, indicating that the molecule could be confidently identified with a dedicated multi-wavelength study.

The retrieval constraints are given in Extended Data Table 2. CO is found to have abundances of $10^{-2.7\pm0.4}$, which is slightly low relative to 40× solar values derived from H_2O. Although low, the uncertainty on the CO abundance is large as the feature is subtle in the data and H_2O and clouds help mask the signature. A confounding factor regarding CO is an RLB effect[17,50], where CO present in the stellar spectra dilutes the strong molecular line cores in the planetary transmission spectrum. This does not affect H_2O, CH_4 or CO_2 as those molecules are not present in the stellar photosphere. In this work, we applied a correction for the CO abundance to account for the RLB effect.

Overall, we find a good fit to the data with a $\chi^2_\nu = 1.1$ for 566 degrees of freedom and 10 free parameters. Our retrieval results are given in Extended Data Table 2 and Extended Data Fig. 4. To estimate the detection confidence of each molecule identified, we re-ran the retrieval leaving out the molecule in question and computed the detection significance using the Bayesian evidence between the models with and without the molecule. We report the results in which H_2S and NH_3 are included in the model, although the G395H data are not sufficient to detect either species confidently. We report the abundances and detection significances from the ATMO results, as they can be directly used to compare against the non-equilibrium models presented in the main text.

ATMO WASP-107b forward non-equilibrium chemistry models. It is computationally infeasible to currently run the ATMO retrieval with the full non-equilibrium photochemistry self-consistently computed at every model evaluation 'on the fly'. Instead, we adopt a two-step grid-retrieval approach, first computing a grid of non-equilibrium chemistry values that are then fit against the retrieved VMR abundances. As we use the same ATMO model setup for both the forward and retrieval modelling, the abundances computed between them can be self-consistently compared.

Our use of a 1D atmospheric model to interpret the non-equilibrium chemistry has several assumptions. The first is that the atmosphere can be considered 1D and is independent of both latitude and longitude. Hot and ultra-hot Jupiters show large day–night temperature gradients[87]. Spitzer phase curves show these differences decrease at lower T_{eq} (ref. 88). Thus, the latitude and longitude temperature differences for warm about 750 K planets such as WASP-107b are expected to be modest. Another important assumption is that the parameters of T_{int} and K_{zz} are constant and assumed to be uniform with depth. Our model contains a single convective region (Extended Data Fig. 6), although the possibility of a separate low-pressure convective zone has been studied[89]. Multiple convective regions would affect our interpretation of T_{int} and the link between atmospheric and interior constraints. Furthermore, our modelling also assumes a single K_{zz} value that is constant with altitude. Theoretical studies have predicted that K_{zz} increases with altitude[20]. Higher K_{zz} values at higher altitudes would not greatly affect our results, as the quench pressures for the molecular features probed here are similar (Extended Data Fig. 6). However, if multiple convective zones are present, the use of a single K_{zz} value may have to be re-visited.

To estimate the parameter space needed for the grid, we first used a chemical equilibrium model[90] and assumed a single quench pressure to estimate the posterior distribution of temperature, pressure, metallicity and C/O ratio parameters that are consistent with the retrieved abundances (Extended Data Fig. 5). This equilibrium model indicated metallicities near 50× solar, C/O ratios near 0.5 and temperatures near 1,000 K at pressures just below a bar are needed to fit the observed molecular abundances. These temperatures are reached at 1 bar only if the planet has an intrinsic temperature greater than about 300 K with super-solar metallicities (Extended Data Fig. 6). Intrinsic temperatures lower than 300 K are ruled out as CH_4 becomes too abundant in the deep atmosphere, such that no amount of mixing could sufficiently deplete the molecule. We also estimate a limit on K_{zz} to be less than $10^{13.5}$ cm^2 s^{-1} based on requiring velocities to be less than the local sound speed. The presence of clouds near millibar pressures also places a lower limit on K_{zz} of about 10^9 cm^2 s^{-1}, as significant vertical mixing is needed to keep the aerosol particles aloft[20].

We input P–T profiles in radiative–convective equilibrium, using intrinsic temperatures (T_{int}) of 300–500 K in steps of 50 K along with a T_{int} of 425 K. With these T–P profiles, we computed the non-equilibrium chemistry as described in ref. 18, using metallicities (Z) between 20× solar and 50× solar in steps of 5×, and 10 log[K_{zz} (cm^2 s^{-1})] values ranging from 11 to 13. A K6V star was used for our input to the photochemical model[91]. Each non-equilibrium model was integrated to 1×10^8 s, which we found was sufficient such that the abundances did not evolve further. We assumed a solar C/O ratio, which is also consistent with WASP-107A from ref. 92 which found values of C/O = 0.5 ± 0.1. We find the C/O ratio does not differ substantially from the solar or host-star value (Extended Data Fig. 5), and we subsequently ran low (0.1 and 0.2) and high (0.7) non-equilibrium chemistry cases that did not improve the fits.

For this grid of models, we then calculated the χ^2 for each grid model, using the retrieved abundances for H_2O, CO, CO_2, CH_4 and SO_2 in Extended Data Table 2. We did not use the H_2S or NH_3 abundances, as they are not fully supported by the data and the errors in any case are large. The best-fit model has a good χ^2 of 4.1 when fitting the five abundances with three grid parameters (Fig. 3 and Extended Data Fig. 7). The grid-posterior can be seen in Extended Data Fig. 7, in which each model was given a weight proportional to its probability, P, calculated as $P = e^{-\chi^2/2}$. From the marginalized grid-posterior, we fit a Gaussian to the distributions and report the fitted $Z/Z_\odot$, T_{int} and K_{zz} values in Extended Data Table 2.

We find the molecular constraints highly constraining for both T_{int} and K_{zz}. Lower vertical mixing rates, generally, require higher intrinsic temperatures to deplete CH_4 to similar values. However, if T_{int} becomes too high, it over-depletes CH_4 relative to CO_2. Moreover, SO_2 helps provide an upper bound on K_{zz} as SO_2 is sensitive to both the photochemistry, needed to produce the species at low pressures, and vertical mixing. Higher values of K_{zz} mix the species from deeper pressures at which the abundances are lower, whereas lower K_{zz} values allow the photochemistry to build up the species near 0.1 mbar pressures.

NEMESIS free retrievals. NEMESIS is a free-chemistry radiative transfer and retrieval code, initially developed for solar system applications[93]. It couples a correlated-k[59] radiative transfer scheme with the PyMultiNest[70–72,94] Nested Sampling algorithm[95]. It has been extensively applied to spectra of hot Jupiter exoplanets[96–98].

The retrievals for WASP-107b incorporate abundances of the gases H_2O (line data[99]), CO_2 (ref. 100), CO (ref. 101), CH_4 (ref. 102), SO_2 (ref. 86), NH_3 (ref. 103), HCN (ref. 104) and H_2S (ref. 105). For each of the gas abundances, we specify a log-uniform prior spanning 10^{-12}–$10^{-0.5}$. The rest of the atmosphere is composed of H_2 and He with a ratio of 0.8547:0.1453. CIA for H_2 and He is taken from refs. 106,107.

Other retrieved properties are an isothermal temperature with a uniform prior and a range of 300–1,000 K, and a grey cloud-top pressure with a log-uniform prior and a range of 10^{-8}–100 bars. We also retrieve the planetary radius at a reference pressure of 100 bars. The retrieved abundances are given in Extended Data Table 2. Additional retrievals were run that had a more flexible T–P profile along with retrievals with patchy clouds and enstatite clouds, although they were not favoured statistically over the simpler model.

Interior structure models. The constraints we found for the intrinsic temperature of WASP-107b have important implications for the interior structure of the planet. To investigate these, we use the interior structure models of ref. 39, revised to use the H/He EOS[108] and parameterize the amount of metal in the core versus mixed into the envelope. As in ref. 39, we assume the metal is a 50–50 mixture of rock and ice.

To match our models to WASP-107b, we use a Bayesian retrieval approach similar to the one used in ref. 109. However, our measurement of T_{int} determines the thermal state of the plane rather than thermal evolution. The parameters of the statistical model were, therefore, the mass of the planet M, the metallicity of the envelope Z_e (a mass fraction), the core mass M_c and the specific entropy of the envelope s. From these, our forward model calculates the radius and T_{int} of the planet. The model was constrained by four normally distributed observations: the mass, the radius, the atmospheric metallicity and T_{int}. These are constraining enough that we can choose very uninformative priors to keep the parameters inside model bounds: a uniform mass prior from

0.01 to 30 M_J, a uniform Z_{env} from 0 to 1, a uniform core mass from 0 to M_J (thus conditional on M but still proper) and a uniform entropy prior from 5 to 11 k_b per baryon. We sampled from the posterior using the Metropolis–Hastings Markov chain Monte Carlo algorithm and verified convergence with the auto-correlation plots and the Gelman–Rubin statistic[110].

Our interior model retrievals (Extended Data Fig. 8) find a planet that contains similar amounts of H/He compared with heavier elements, with $Z_p = 0.608 \pm 0.046$. This seems reasonable for a planet of this mass: it accreted a substantial amount of material from the disk, but never reached the runaway gas accretion stage. However, this is in contrast to the previous estimates of the composition of the planet, which saw it as having substantially larger quantities of H/He: that is, more than 85% H/He from ref. 10. This is because our measured T_{int} is much hotter than a standard thermal evolution model would suggest; we would expect the planet to have cooled below our 2σ lower bound of 300 K within tens of Myr of formation. Instead, it is clear that the planet is being inflated by an extra heat source despite being too cool to experience hot Jupiter-type inflation[111]. Instead, a mechanism such as tidal heating[112–114], previously suspected to be operating on WASP-107b (refs. 10,115), is warming the interior. These models propose that the eccentricity of WASP-107b is excited by WASP-107 c, but then damped out through tidal interaction with the star; the resulting energy is deposited in the interior of the planet. Our large measured T_{int} is evidence that this process could be occurring, with a precise eccentricity further capable of constraining the mechanism.

Another interesting result of our interior structure models is that it puts constraints on the mass of the core of the planet. The mass, radius and T_{int} already constrain the overall metallicity of the planet (more metal means a smaller planet) to $Z_p = 0.635^{+0.104}_{-0.085}$, but we also have a measurement of the atmospheric metallicity of the planet. This enables us to make a modestly better constraint on Z (see previous paragraph); more importantly, metal seen in the bulk but not in the atmosphere must be hidden in the interior in a core or composition layers (see ref. 109 for further discussion). Assuming a uniform composition core gives us $M_c = 11.5^{+3.01}_{-3.58} M_\oplus$. This range excludes zero, meaning that we have detected the presence of a core. The exact structure of the interior may not be exactly an envelope-on-core model, but may be more like Neptune and Uranus with a rocky core, water envelope, than a H/He envelope[36]. Alternatively, the core may be diffuse and/or layered as the core of Jupiter is thought to be[37,38]. Nevertheless, our result that a core exists is not affected by these possibilities: we cannot propose a layered core without a core in the first place.

Data availability

The data used in this paper are associated with the JWST programme GO 1224 (PI Birkmann) and are publicly available from the Mikulski Archive for Space Telescopes (https://mast.stsci.edu) from 23 June 2024. The data products in Figs. 1, 2 and 3 are available at Zenodo (https://doi.org/10.5281/zenodo.10891400) (ref. 116). Source data are provided with this paper.

Code availability

The codes used in this publication to extract, reduce and analyse the data are as follows: STScI JWST Calibration pipeline (https://github.com/spacetelescope/jwst) and FIREFLy[17,42]. Moreover, these codes made use ExoTiC-LD[117] (https://exotic-ld.readthedocs.io/en/latest/) and Emcee (https://emcee.readthedocs.io/en/stable/)[118], which use the Python libraries scipy[119], numpy[120], astropy[121] and matplotlib[122]. Model and retrievals were generated using ATMO, a proprietary code extensively described in refs. 18,32,51–54 and NEMESIS[93] (https://github.com/nemesiscode/radtrancode).

42. Rustamkulov, Z., Sing, D. K., Liu, R. & Wang, A. Analysis of a JWST NIRSpec lab time series: characterizing systematics, secovering exoplanet transit spectroscopy, and constraining a noise floor. *Astrophys. J. Lett.* **928**, L7 (2022).
43. Kipping, D. M. Efficient, uninformative sampling of limb darkening coefficients for two-parameter laws. *Mon. Not. R. Astron. Soc.* **435**, 2152–2160 (2013).
44. Magic, Z., Chiavassa, A., Collet, R. & Asplund, M. The STAGGER-grid: a grid of 3D stellar atmosphere models. IV. Limb darkening coefficients. *Astron. Astrophys.* **573**, A90 (2015).
45. Bushouse, H. et al. JWST Calibration Pipeline (v.1.14.0). GitHub https://github.com/spacetelescope/jwst (2024).
46. Miller, T. et al. CRDS: Calibration Reference Data System for HST and JWST. GitHub github.com/spacetelescope/crds (2022).
47. Foreman-Mackey, D. et al. Exoplanet: gradient-based probabilistic inference for exoplanet data & other astronomical time series. *J. Open Source Softw.* **6**, 3285 (2021).
48. Foreman-Mackey, D. et al. exoplanet-dev/exoplanet v0.5.1rc1. Zenodo https://doi.org/10.5281/zenodo.5006644 (2021).
49. Morello, G. et al. The ExoTETHyS package: tools for exoplanetary transits around host stars. *Astron. J.* **159**, 75 (2020).
50. Deming, D. & Sheppard, K. Spectral resolution-linked bias in transit spectroscopy of extrasolar planets. *Astrophys. J. Lett.* **841**, L3 (2017).
51. Amundsen, D. S. et al. Accuracy tests of radiation schemes used in hot Jupiter global circulation models. *Astron. Astrophys.* **564**, A59 (2014).
52. Tremblin, P. et al. Fingering convection and cloudless models for cool brown dwarf atmospheres. *Astrophys. J. Lett.* **804**, L17 (2015).
53. Tremblin, P. et al. Cloudless atmospheres for L/T dwarfs and extrasolar giant planets. *Astrophys. J. Lett.* **817**, L19 (2016).
54. Goyal, J. M. et al. A library of ATMO forward model transmission spectra for hot Jupiter exoplanets. *Mon. Not. R. Astron. Soc.* **474**, 5158–5185 (2018).
55. Edwards, J. M. & Slingo, A. Studies with a flexible new radiation code. I: choosing a configuration for a large-scale model. *Q. J. R. Meteorol. Soc.* **122**, 689–719 (1996).
56. Baudino, J.-L. et al. Interpreting the photometry and spectroscopy of directly imaged planets: a new atmospheric model applied to β Pictoris b and SPHERE observations. *Astron. Astrophys.* **582**, A83 (2015).
57. Mollière, P., van Boekel, R., Dullemond, C., Henning, T. & Mordasin, C. Model atmospheres of irradiated exoplanets: the influence of stellar parameters, metallicity, and the C/O ratio. *Astrophys. J.* **813**, 47 (2015).
58. Baudino, J.-L. et al. Toward the analysis of JWST exoplanet spectra: identifying troublesome model parameters. *Astrophys. J.* **850**, 150 (2017).
59. Lacis, A. A. & Oinas, V. A description of the correlated-k distribution method for modelling nongray gaseous absorption, thermal emission, and multiple scattering in vertically inhomogeneous atmospheres. *J. Geophys. Res.* **96**, 9027–9064 (1991).
60. Goyal, J. M. et al. A library of self-consistent simulated exoplanet atmospheres. *Mon. Not. R. Astron. Soc.* **498**, 4680–4704 (2020).
61. Gordon, S. & McBride, B. J. *Computer Program for Calculation of Complex Chemical Equilibrium Compositions and Applications. I. Analysis*. NASA Reference Publication 1311 (NASA, 1994).
62. McBride, B. J., Gordon, S. & Reno, M. A. *Coefficients for Calculating Thermodynamic and Transport Properties of Individual Species*. NASA Technical Memorandum 4513 (NASA, 1993).
63. Asplund, M., Grevesse, N., Sauval, A. J. & Scott, P. The chemical composition of the sun. *Annu. Rev. Astron.* **47**, 481–522 (2009).
64. Caffau, E., Ludwig, H.-G., Steffen, M., Freytag, B. & Bonifacio, P. Solar chemical abundances determined with a CO5BOLD 3D model atmosphere. *Sol. Phys.* **268**, 255–269 (2011).
65. Goyal, J. M. et al. Fully scalable forward model grid of exoplanet transmission spectra. *Mon. Not. R. Astron. Soc.* **482**, 4503–4513 (2019).
66. Venot, O. et al. A chemical model for the atmosphere of hot Jupiters. *Astron. Astrophys.* **546**, A43 (2012).
67. Tsai, S.-M. et al. A comparative study of atmospheric chemistry with VULCAN. *Astrophys. J.* **923**, 264 (2021).
68. Venot, O. et al. New chemical scheme for giant planet thermochemistry: update of the methanol chemistry and new reduced chemical scheme. *Astron. Astrophys.* **634**, A78 (2020).
69. Lecavelier des Etangs, A., Pont, F., Vidal-Madjar, A. & Sing, D. Rayleigh scattering in the transit spectrum of HD 189733b. *Astron. Astrophys.* **481**, L83–L86 (2008).
70. Feroz, F. & Hobson, M. P. Multimodal nested sampling: an efficient and robust alternative to Markov Chain Monte Carlo methods for astronomical data analyses. *Mon. Not. R. Astron. Soc.* **384**, 449–463 (2008).
71. Feroz, F., Hobson, M. P. & Bridges, M. MULTINEST: an efficient and robust Bayesian inference tool for cosmology and particle physics. *Mon. Not. R. Astron. Soc.* **398**, 1601–1614 (2009).
72. Feroz, F., Hobson, M. P., Cameron, E. & Pettitt, A. N. Importance nested sampling and the MultiNest algorithm. *Open J. Astrophys.* **2**, 10 (2019).
73. Evans, T. M. et al. An ultrahot gas-giant exoplanet with a stratosphere. *Nature* **548**, 58–61 (2017).
74. Wakeford, H. R. et al. HAT-P-26b: a Neptune-mass exoplanet with a well-constrained heavy element abundance. *Science* **356**, 628–631 (2017).
75. Spake, J. J. et al. Helium in the eroding atmosphere of an exoplanet. *Nature* **557**, 68–70 (2018).
76. Nikolov, N. et al. An absolute sodium abundance for a cloud-free 'hot Saturn' exoplanet. *Nature* **557**, 526–529 (2018).
77. Carter, A. L. et al. Detection of Na, K, and H_2O in the hazy atmosphere of WASP-6b. *Mon. Not. R. Astron. Soc.* **494**, 5449–5472 (2020).
78. Line, M. R. et al. Information content of exoplanetary transit spectra: an initial look. *Astrophys. J.* **749**, 93 (2012).
79. Guillot, T. On the radiative equilibrium of irradiated planetary atmospheres. *Astron. Astrophys.* **520**, A27 (2010).
80. Barber, R. J., Tennyson, J., Harris, G. J. & Tolchenov, R. N. A high-accuracy computed water line list. *Mon. Not. R. Astron. Soc.* **368**, 1087–1094 (2006).

81. Tashkun, S. A. & Perevalov, V. I. CDSD-4000: high-resolution, high-temperature carbon dioxide spectroscopic databank. *J. Quant. Spectrosc. Radiat. Transf.* **112**, 1403–1410 (2011).
82. Rothman, L. et al. HITEMP, the high-temperature molecular spectroscopic database. *J. Quant. Spectros. Radiat. Transf.* **111**, 2139–2150 (2010).
83. Yurchenko, S. N. & Tennyson, J. ExoMol line lists – IV. The rotation–vibration spectrum of methane up to 1500 K. *Mon. Not. R. Astron. Soc.* **440**, 1649–1661 (2014).
84. Yurchenko, S. N., Barber, R. J. & Tennyson, J. A variationally computed line list for hot NH_3. *Mon. Not. R. Astron. Soc.* **413**, 1828–1834 (2011).
85. Rothman, L. et al. The HITRAN2012 molecular spectroscopic database. *J. Quant. Spectrosc. Radiat. Transf.* **130**, 4–50 (2013).
86. Underwood, D. S. et al. ExoMol molecular line lists – XIV. The rotation–vibration spectrum of hot SO_2. *Mon. Not. R. Astron. Soc.* **459**, 3890–3899 (2016).
87. Mikal-Evans, T. et al. Diurnal variations in the stratosphere of the ultrahot giant exoplanet WASP-121b. *Nat. Astron.* **6**, 471–479 (2022).
88. Bell, T. J. et al. A comprehensive reanalysis of *Spitzer*'s 4.5 μm phase curves, and the phase variations of the ultra-hot Jupiters MASCARA-1b and KELT-16b. *Mon. Not. R. Astron. Soc.* **504**, 3316–3337 (2021).
89. Guillot, T. & Showman, A. P. Evolution of "51 Pegasus b-like" planets. *Astron. Astrophys.* **385**, 156–165 (2002).
90. Cubillos, P., Blecic, J. & Fossati, L. Radiative and thermochemical equilibrium calculations and application for warm-Jupiter exoplanets. https://github.com/AtmoLib/chemcat (2024).
91. France, K. et al. The MUSCLES Treasury Survey. I. Motivation and Overview. *Astrophys. J.* **820**, 89 (2016).
92. Hejazi, N. et al. Elemental abundances of the super-Neptune WASP-107b's host star using high-resolution, near-infrared spectroscopy. *Astrophys. J.* **949**, 79 (2023).
93. Irwin, P. G. J. et al. The NEMESIS planetary atmosphere radiative transfer and retrieval tool. *J. Quant. Spectrosc. Radiat. Transf.* **109**, 1136–1150 (2008).
94. Buchner, J. et al. X-ray spectral modelling of the AGN obscuring region in the CDFS: Bayesian model selection and catalogue. *Astron. Astrophys.* **564**, A125 (2014).
95. Krissansen-Totton, J., Garland, R., Irwin, P. & Catling, D. C. Detectability of Biosignatures in Anoxic Atmospheres with the *James Webb Space Telescope*: a TRAPPIST-1e case study. *Astrophys. J.* **156**, 114 (2018).
96. Barstow, J. K., Aigrain, S., Irwin, P. G. J. & Sing, D. K. A consistent retrieval analysis of 10 hot Jupiters observed in transmission. *Astrophys. J.* **834**, 50 (2017).
97. Lewis, N. K. et al. Into the UV: the atmosphere of the hot Jupiter HAT-P-41b revealed. *Astrophys. J. Lett.* **902**, L19 (2020).
98. Rathcke, A. D. et al. HST PanCET Program: a complete near-UV to infrared transmission spectrum for the hot Jupiter WASP-79b. *Astrophys. J.* **162**, 138 (2021).
99. Polyansky, O. L. et al. ExoMol molecular line lists XXX: a complete high-accuracy line list for water. *Mon. Not. R. Astron. Soc.* **480**, 2597–2608 (2018).
100. Yurchenko, S. N., Mellor, T. M., Freedman, R. S. & Tennyson, J. ExoMol line lists – XXXIX. Ro-vibrational molecular line list for CO_2. *Mon. Not. R. Astron. Soc.* **496**, 5282–5291 (2020).
101. Li, G. et al. Rovibrational line lists for nine isotopologues of the CO molecule in the $X^1\Sigma^+$ ground electronic state. *Astrophys. J. Suppl. Ser.* **216**, 15 (2015).
102. Yurchenko, S. N., Amundsen, D. S., Tennyson, J. & Waldmann, I. P. A hybrid line list for CH_4 and hot methane continuum. *Astron. Astrophys.* **605**, A95 (2017).
103. Coles, P. A., Yurchenko, S. N. & Tennyson, J. ExoMol molecular line lists – XXXV. A rotation–vibration line list for hot ammonia. *Mon. Not. R. Astron. Soc.* **490**, 4638–4647 (2019).
104. Barber, R. J. et al. ExoMol line lists – III. An improved hot rotation-vibration line list for HCN and HNC. *Mon. Not. R. Astron. Soc.* **437**, 1828–1835 (2014).
105. Azzam, A. A. A., Tennyson, J., Yurchenko, S. N. & Naumenko, O. V. ExoMol molecular line lists - XVI. The rotation-vibration spectrum of hot H_2S. *Mon. Not. R. Astron. Soc.* **460**, 4063–4074 (2016).
106. Borysow, A., Jorgensen, U. G. & Fu, Y. High-temperature (1000-7000 K) collision-induced absorption of H_2 pairs computed from the first principles, with application to cool and dense stellar atmospheres. *J. Quant. Spectrosc. Radiat. Transf.* **68**, 235–255 (2001).
107. Borysow, A. Collision-induced absorption coefficients of H_2 pairs at temperatures from 60 K to 1000 K. *Astron. Astrophys.* **390**, 779–782 (2002).
108. Chabrier, G., Mazevet, S. & Soubiran, F. A new equation of state for dense hydrogen-helium mixtures. *Astrophys. J.* **872**, 51 (2019).
109. Thorngren, D. & Fortney, J. J. Connecting giant planet atmosphere and interior modeling: constraints on atmospheric metal enrichment. *Astrophys. J. Lett.* **874**, L31 (2019).
110. Gelman, A. & Rubin, D. B. Inference from iterative simulation using multiple sequences. *Stat. Sci.* **7**, 457–472 (1992).
111. Miller, N. & Fortney, J. J. The heavy-element masses of extrasolar giant planets, revealed. *Astrophys. J. Lett.* **736**, L29 (2011).
112. Bodenheimer, P. & Lin, D. N. C. Implications of extrasolar planets for understanding planet formation. *Annu. Rev. Earth Planet. Sci.* **30**, 113–148 (2002).
113. Jackson, B., Greenberg, R. & Barnes, R. Tidal heating of extrasolar planets. *Astrophys. J.* **681**, 1631–1638 (2008).
114. Millholland, S. Tidally induced radius inflation of sub-Neptunes. *Astrophys. J.* **886**, 72 (2019).
115. Millholland, S., Petigura, E. & Batygin, K. Tidal inflation reconciles low-density sub-Saturns with core accretion. *Astrophys. J.* **897**, 7 (2020).
116. Sing, D. Products for "A warm Neptune's methane reveals core mass and vigorous atmospheric mixing". Zenodo https://doi.org/10.5281/zenodo.10891400 (2024).
117. Grant, D. & Wakeford, H. R. Exo-TiC/ExoTiC-LD: ExoTiC-LD v3.0.0. Zenodo https://doi.org/10.5281/zenodo.7437681 (2022).
118. Foreman-Mackey, D., Hogg, D. W., Lang, D. & Goodman, J. emcee: the MCMC hammer. *Publ. Astron. Soc. Pacif.* **125**, 306–312 (2013).
119. Virtanen, P. et al. SciPy 1.0: fundamental algorithms for scientific computing in Python. *Nat. Methods* **17**, 261–272 (2020).
120. Harris, C. R. et al. Array programming with NumPy. *Nature* **585**, 357–362 (2020).
121. Astropy Collaboration et al. The Astropy Project: building an open-science project and status of the v2.0 core package. *Astron. J.* **156**, 123 (2018).
122. Hunter, J. D. Matplotlib: a 2D graphics environment. *Comput. Sci. Eng.* **9**, 90–95 (2007).
123. Deming, D. et al. Emergent spectral fluxes of hot Jupiters: an abrupt rise in dayside brightness temperature under strong irradiation. *Astron. J.* **165**, 104 (2023).
124. Dai, F. & Winn, J. N. The oblique orbit of WASP-107b from K2 photometry. *Astron. J.* **153**, 205 (2017).

Acknowledgements This work is based on the observations made with the NASA/ESA/CSA JWST. The data were obtained from the Mikulski Archive for Space Telescopes at the Space Telescope Science Institute, operated by the Association of Universities for Research in Astronomy, under NASA contract NAS 5-03127 for JWST. E.K.H. Lee is supported by the SNSF Ambizione Fellowship grant (#193448). J.K.B. is supported by UK Research and Innovation via an STFC Ernest Rutherford Fellowship (ST/T004479/1).

Author contributions D.K.S. led the data analysis and modelling. Z.R., N.E. and N.C. provided data analysis and input. J.K.B., Z.R. provided atmospheric models. D.P.T. provided planetary interior models. S.M.B. led the observational setup and execution of the program. R.C.C., N.K.L. and E.K.H.L provided support interpreting the results. C.A.d.O., T.L.B., S.M.B., P.F., G.G., R.M., E.M., B.J.R., M.S., A.G. and J.A.V. contributed to the NIRSpec instrument and GTO team. The manuscript was written by D.K.S. along with D.P.T., J.K.B. and P.T.

Competing interests The authors declare no competing interests.

Additional information

Supplementary information The online version contains supplementary material available at https://doi.org/10.1038/s41586-024-07395-z.

Correspondence and requests for materials should be addressed to David K. Sing.

Peer review information *Nature* thanks Drake Deming and Tristan Guillot for their contribution to the peer review of this work. Peer reviewer reports are available.

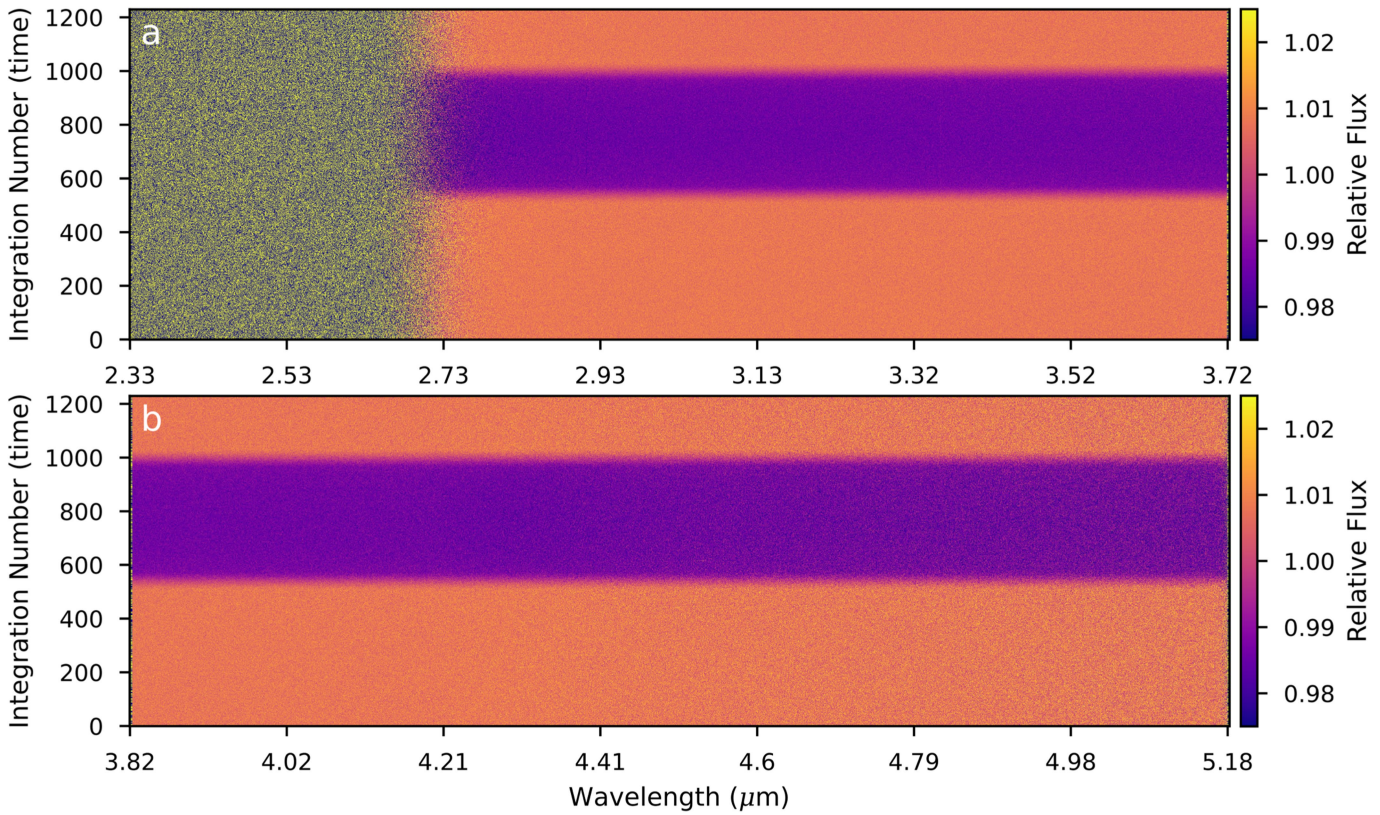

Extended Data Fig. 1 | FIREFLy transit light curve spectrophotometry. Shown is the relative flux as a function of wavelength and time for NIRSpec detectors (**a**) NRS1 and (**b**) NRS2.

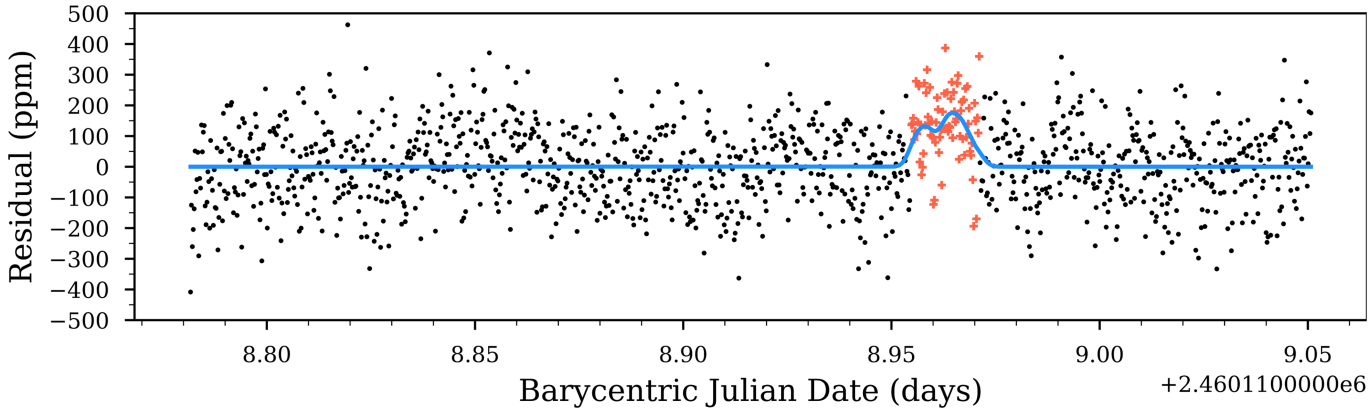

Extended Data Fig. 2 | Stellar spot-crossing. Shown is the residual white-light curve photometry from NRS1 when fitting for the non-spotted data (black dots). The suspected occulted spot (red crosses) is shown, with a Gaussian smoothed filter overplotted (blue line).

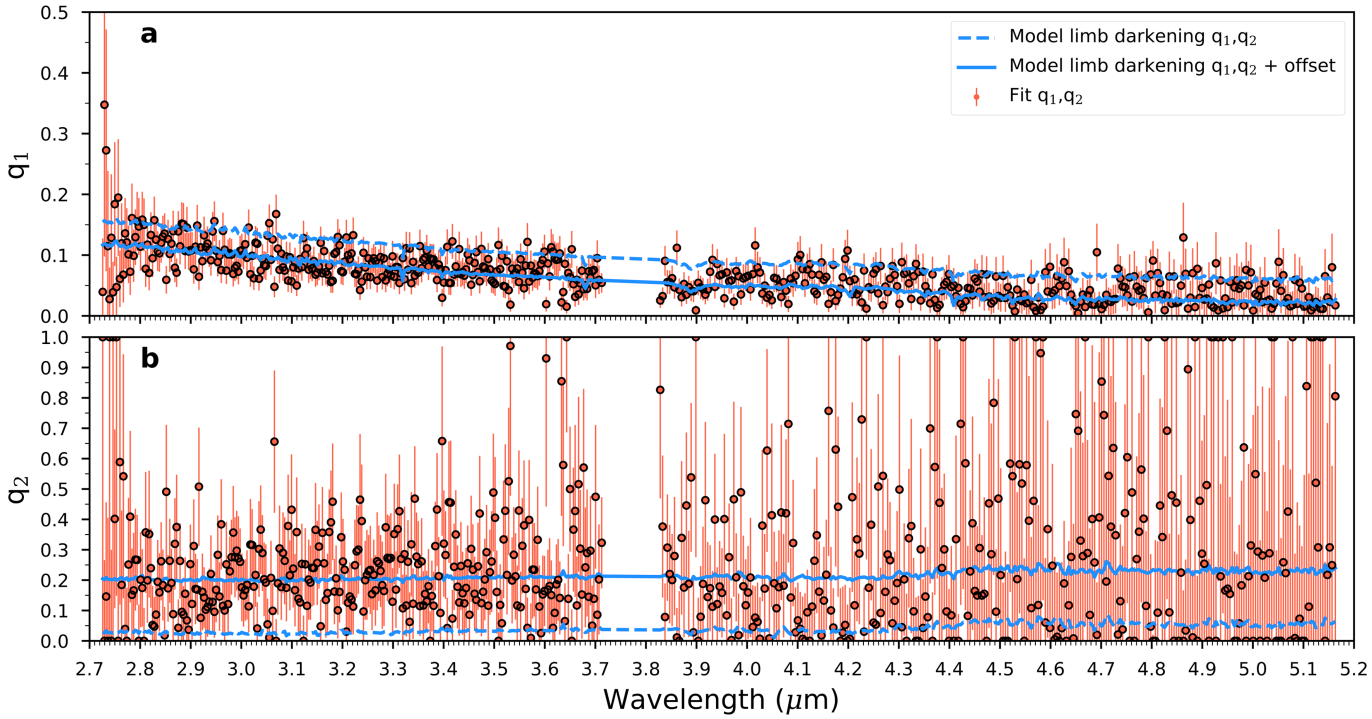

Extended Data Fig. 3 | Limb-Darkening. Shown are the resulting stellar limb-darkening coefficients q_1 (**a**) and q_2 (**b**) derived from the transit light curves using a quadratic law. The limb-darkening coefficients derived from a stellar model are also shown, along with the models with an offset derived from the difference between the data and model.

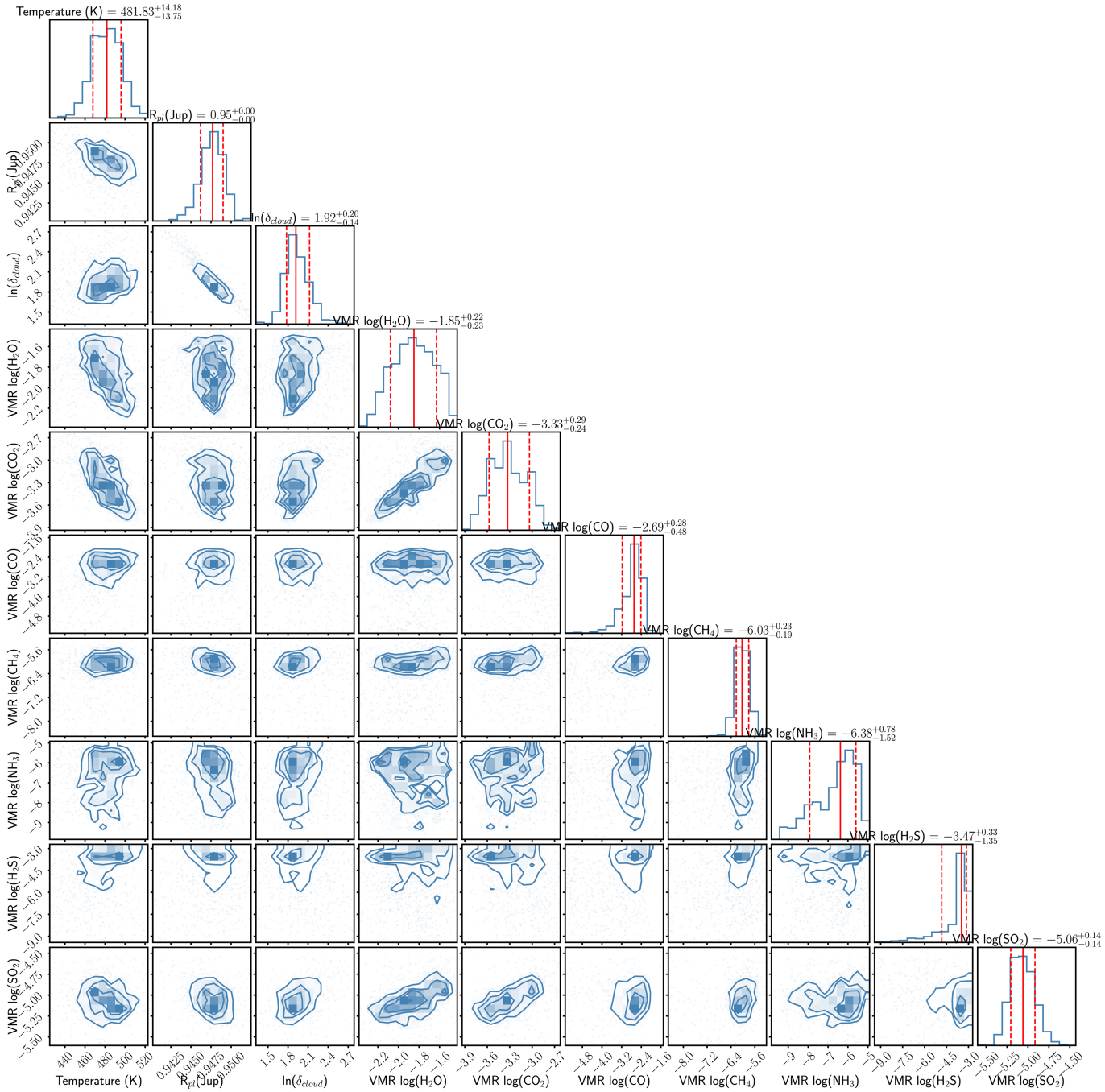

Extended Data Fig. 4 | WASP-107 b retrieval posteriors. Shown is the distribution for the ATMO free-retrieval. VMR refers to the Volume Mixing Ratio of the molecular species. 1, 1.5, and 2-σ equivalent contours are shown. The 1D histograms show the marginalized parameter median value and 1-σ range (red).

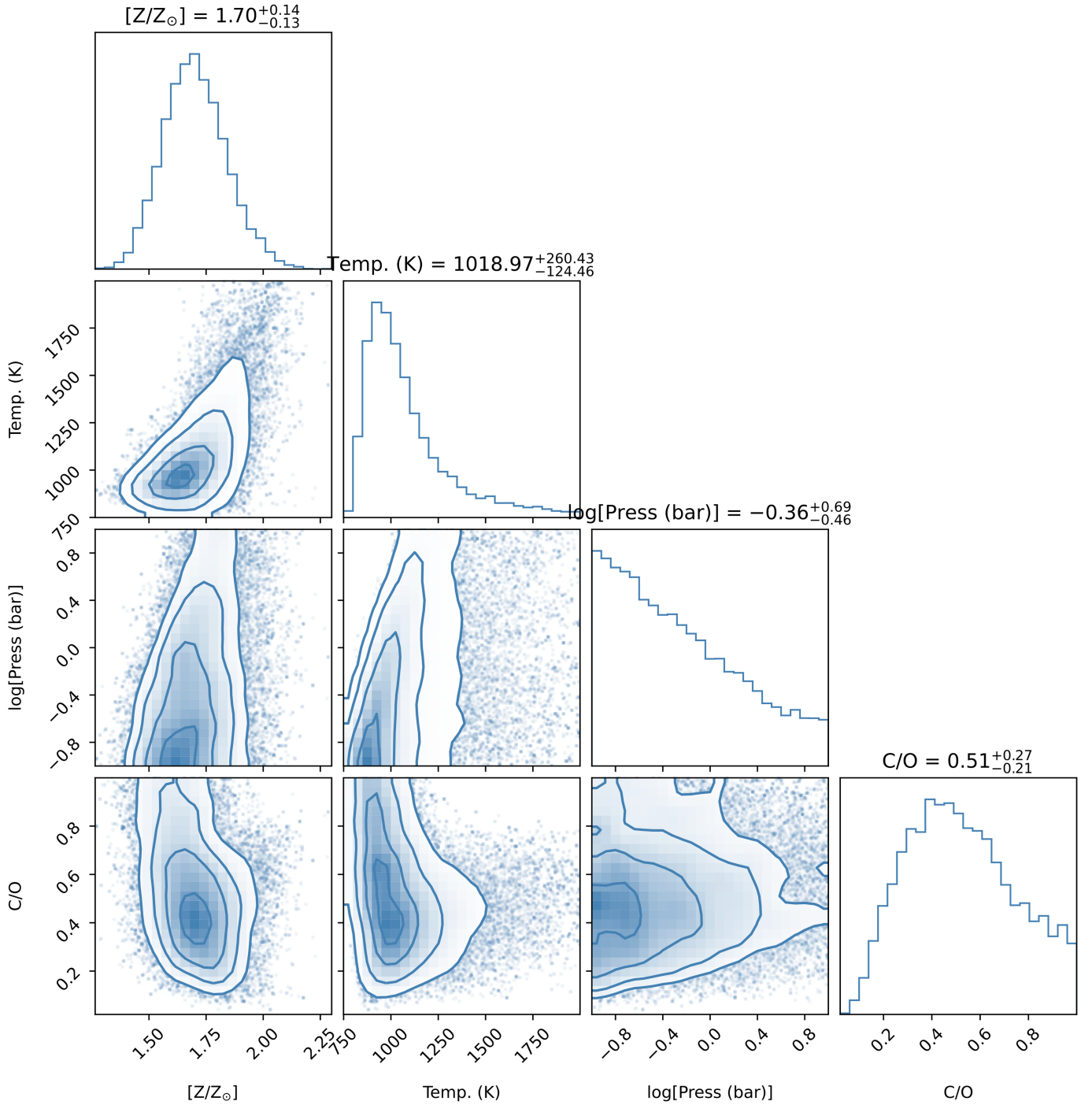

Extended Data Fig. 5 | Equilibrium chemistry estimation. Shown is a posterior distribution of metallicity, temperature, pressure and C/O equilibrium chemistry[90] values that are simultaneously compatible with the retrieved abundances of H_2O, CO, CO_2.

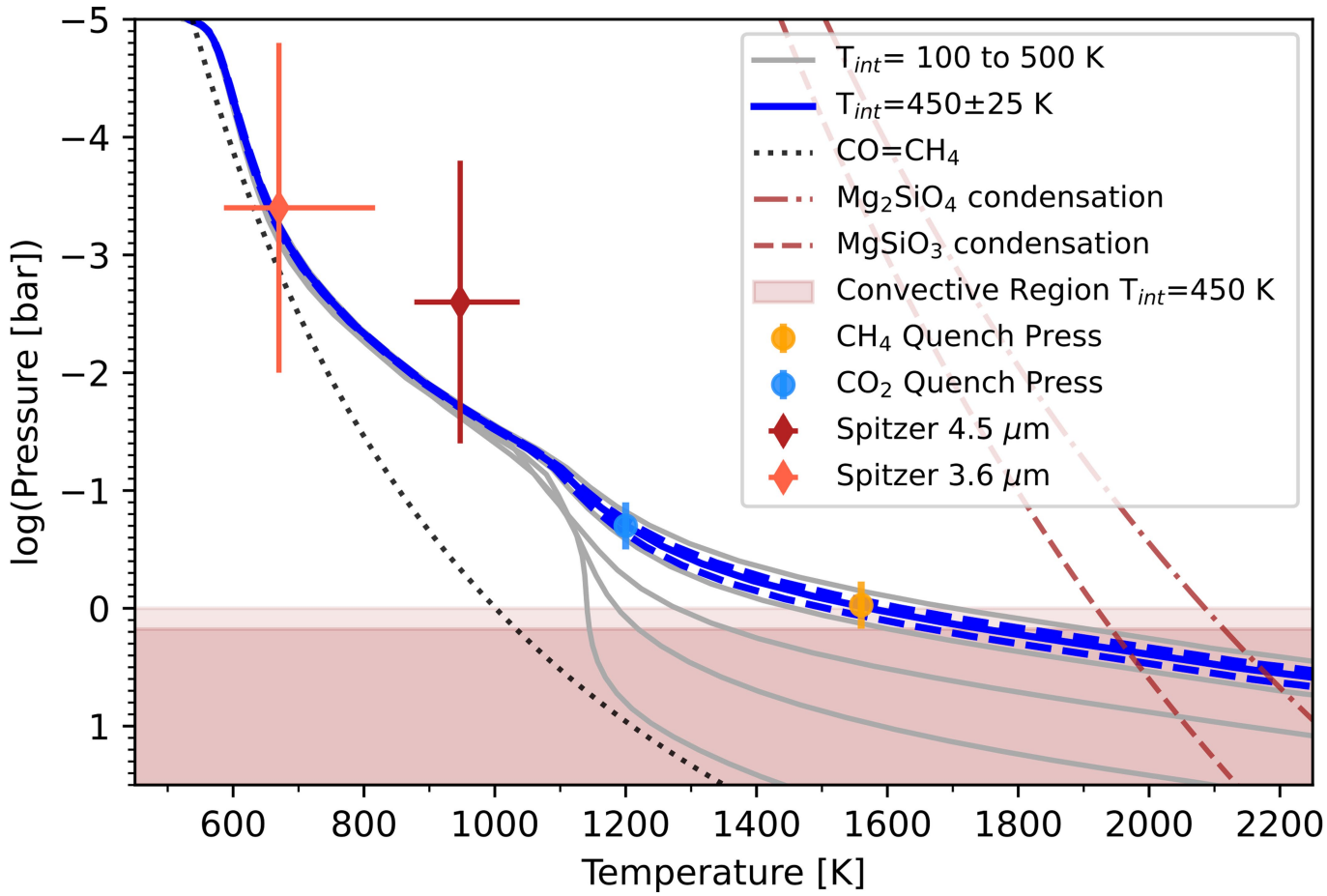

Extended Data Fig. 6 | Pressure-Temperature Profiles. Shown are P-T profiles in radiative-convective equilibrium with T_{int} values ranging from 100 to 500 K (grey). The T-P with the best-fit T_{int} is shown (blue), with a shaded region showing where the model is dominated by convection. The quench pressures for CO_2 and CH_4 are also depicted along with Mg-Si condensation curves (dashed, dot dashed lines). The equilibrium CH_4=CO equal-abundance curve is also shown (dotted line), with the CH_4 abundance dropping at increased temperatures. The brightness temperatures measured from Spitzer secondary eclipse observations are shown from ref. 123. The corresponding pressures and ranges are derived from the best-fit model contribution function, with the y-axis range encapsulating 80% of the total emitted flux. The Spitzer brightness temperatures are consistent with the best-fitting T_{int} = 460*K* T-P profile.

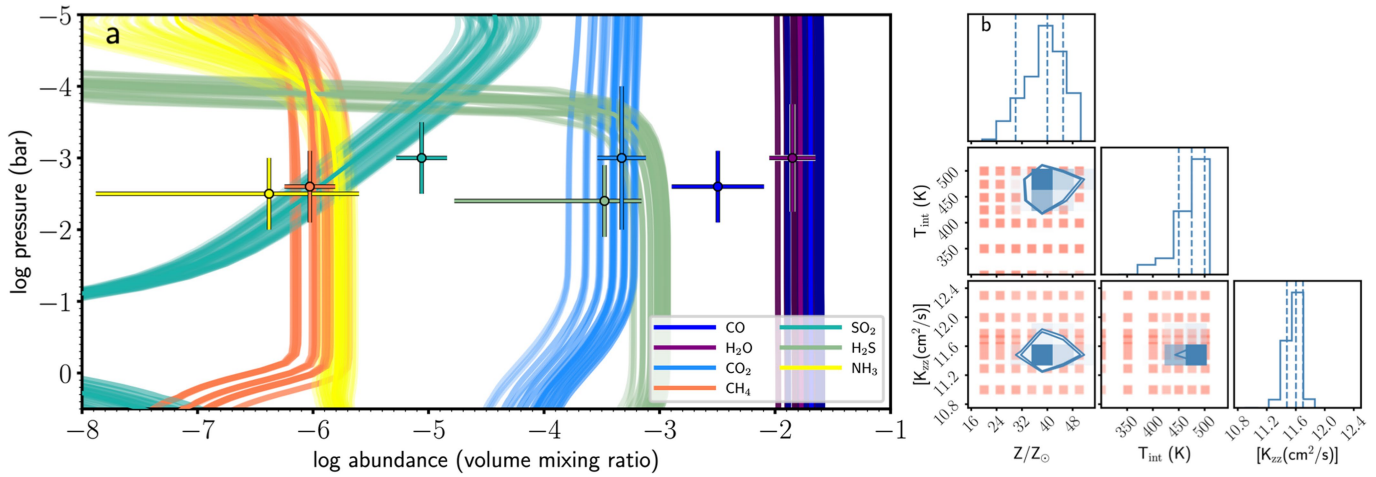

Extended Data Fig. 7 | WASP-107b forward non-equilibrium chemistry model grid results. (**a**) Shown are the best-fitting chemical abundances (within 1-σ) from the non-equilibrium chemistry models along with the retrieved values from the JWST transmission spectrum (datapoints). (**b**) The corner plot depicts the forward model grid points (red squares) along with the constraints in atmospheric metallicity ($Z/Z_{\odot}$), intrinsic temperature ($T_{\rm int}$), and eddy diffusion coefficient (K_{zz}).

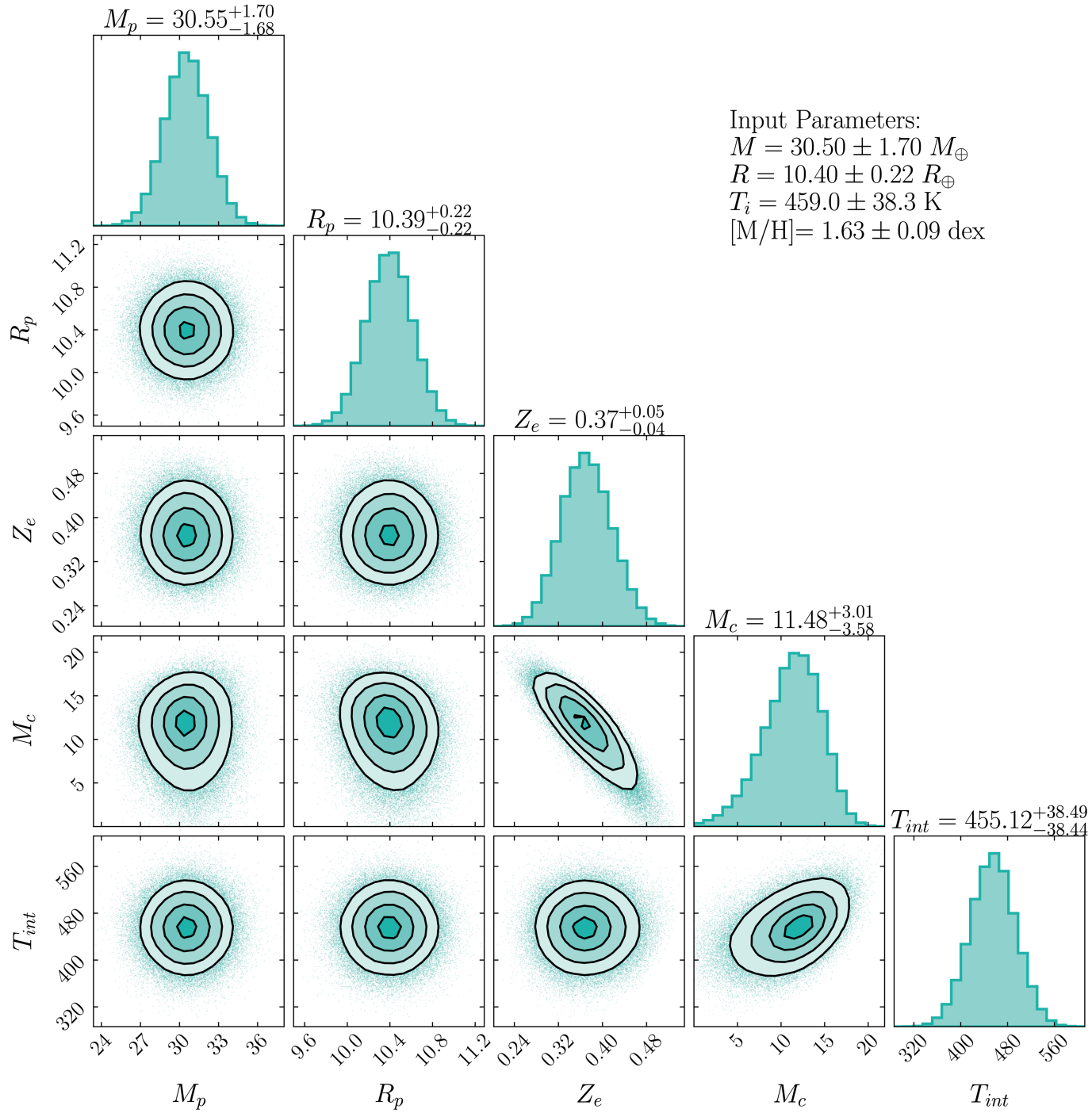

Extended Data Fig. 8 | Interior structure modeling constraints. A corner plot of the posterior mass (M_J), radius (R_J), envelope metallicity (unitless), core mass ($M_\oplus$), and intrinsic temperature (K). The model inputs (from observations) are shown in the upper-right, and the priors were weakly-informative. The overall bulk metallicity is set by M, R, and T_{int}, and can be seen as an arc in Z_e-M_c space. Our atmospheric constraint restricts us to a section of this arc; without it, the two parameters would be fully degenerate, running from $M_c = 0$ on one side to $Z_e = 0$ on the other, though the effect on Z_p would be much more limited. The intrinsic temperature is significantly higher than unheated evolution models would produce, and is thus evidence of tidal heating (see text).

Extended Data Table 1 | Orbital parameters

Parameter	Value	Description	Reference
P	5.7214742±0.0000043		[124]
T_0	$2460118.948861 \pm 0.0000063$	Mid-transit time days ($\mathrm{BJD_{TDB}}$)	this work
$a/R_\star$	18.0923 ± 0.0212	Scaled semi-major axis	this work
b	0.11650 ± 0.01199	Transit impact parameter	this work

Best-fit orbital parameters as measured from the FIREFLy JWST white light curve. Reference 124.

Extended Data Table 2 | Model Results

Parameter	Value & 1-σ Uncertainty	Detection (σ)	Value & 1-σ Uncertainty
	`ATMO` Retrieval		`NEMESIS` Retrieval
Atmosphere Temperature (K)	482^{+14}_{-13}		474^{+17}_{-11}
R_{pl} (R_J)	$0.9477^{+0.0013}_{-0.0015}$ (mbar)		0.88±0.01 (100 bar)
cloud δ_{cloud}	$1.91^{+0.20}_{-0.14}$		
log (cloud top) (bar)			$-3.74^{+0.12}_{-0.16}$
VMR log(H_2O)	$-1.85^{+0.22}_{-0.23}$	17	$-1.72^{+0.26}_{-0.25}$
VMR log(CO)	$-2.70^{+0.28}_{-0.48}$	4	$-3.85^{+0.62}_{-0.87}$
VMR log(CO_2)	$-3.33^{+0.29}_{-0.25}$	43	$-2.62^{+0.36}_{-0.34}$
VMR log(CH_4)	$-6.03^{+0.22}_{-0.20}$	4.2	$-6.14^{+0.42}_{-1.70}$
VMR log(SO_2)	$-5.06^{+0.14}_{-0.15}$	5.5	$-4.59^{+0.19}_{-0.18}$
VMR log(H_2S)	$-3.48^{+0.32}_{-1.35}$	2.0	$-7.10^{+3.18}_{-3.00}$
VMR log(NH_3)	$-6.38^{+0.78}_{-1.54}$	1.5	$-8.12^{+1.99}_{-2.36}$
VMR log(HCN)			$-9.12^{+2.01}_{-1.94}$
	`ATMO` Non-Equilibrium Forward		
Metallicity, $Z/Z_\odot$	43±8		
Intrinsic Temperature, T_{int} (K)	458±38		
Diffusion coeff., log[K_{zz} (cm^2/s)]	11.6±0.1		

The retrieval results from the ATMO and NEMESIS codes are given, with the best-fit parameter values shown along with their 1-σ uncertainties. T_{int} refers to the intrinsic temperature, which is related to the flux, F, emitted from the planet's interior by $F = \sigma_R T_{int}^4$, where σ_R the Stefan-Boltzmann constant. VMR refers to the Volume Mixing Ratio.

Extended Data Table 3 | Aerosol Cloud Retrieval Comparisons

aerosol model	parameters	model selection	VMR CH_4	$\log[K_{zz}\ (cm^2/s)]$
	`ATMO` Retrieval	ΔBIC		
grey cloud	δ_{cloud}	-	$-6.03^{+0.22}_{-0.20}$	11.60 ± 0.11
cloud + haze	δ_{cloud},δ_{haze},α_{haze}	5.0	$-6.29^{+0.19}_{-0.26}$	11.56 ± 0.09
grey cloud	log(cloud top)	5.3	$-5.96^{+0.24}_{-0.25}$	11.47 ± 0.11
	`NEMESIS` Retrieval	Δ(lnBE)		
grey cloud	log(cloud top)	-	$-6.14^{+0.42}_{-1.70}$	
grey cloud	δ_{cloud}	-4.1	$-5.86^{+0.35}_{-0.85}$	
enstatite cloud	δ_{cloud}	-20.0	$-5.38^{+0.23}_{-0.27}$	

BIC refers to the Bayesian information criterion, while BE refers to the Bayesian Evidence. Both statistics are calculated relative to the best-fit model given a value of '-'.